Global teleconnections associated with diabatic heating due to local rainfall events

Master Thesis

submitted in fulfilment of the requirements for the degree

Master of Science (M. Sc.)

Climate Physics: Meteorology and Physical Oceanography

Faculty of Mathematics and Natural Sciences

Christian – Albrechts – Universität zu Kiel

Sandro Dahlke

954253

Supervisor: Prof. Dr. Richard Greatbatch

Second Supervisor: Prof. Dr. Katja Matthes

Kiel, August 2015

Abstract

In this thesis, atmospheric teleconnection patterns and their interannual connection to anomalous local rainfall in the summer and winter season are investigated in the period after 1979. Given the lack of quality of gridded reanalysis rainfall products, especially in the period prior to 1979, an ensemble mean estimate of three satellite-based rainfall products covering 32 years is used as a proxy for diabatic heating in the troposphere. It is shown that the diabatic heating due to local rainfall can affect the tropospheric circulation in regions very distant from the heating, while the induced teleconnections may as well affect global weather and climate. It is argued that planetary waves are responsible for communicating the teleconnections throughout the globe. Hence, anomalous Rossby Wave Sources (RWSs), that are related to the diabatic heating, are shown to drive the teleconnection patterns via generation of vorticity. It is found that the midlatitude jets play an important role for the generation of teleconnections, as they act as waveguides for planetary waves.

The satellite ensemble mean rainfall in the tropical Pacific has good skill in reproducing teleconnections that are associated with El Niño, namely the projection onto the Pacific North American (PNA) pattern and the Pacific South American (PSA) pattern.

It is shown that even when the signal of El Niño and the local SST is removed from the seasonal rainfall everywhere on the globe, there are regions evident, where anomalous rainfall can disturb the troposphere and generate global-scale teleconnections. Thus, anomalous diabatic heating over the central Pacific Ocean generates a westward shifted PNA pattern.

Further, enhanced winter rainfall over the tropical Indian Ocean projects onto the positive phase of the North Atlantic Oscillation (NAO), which is the dominant mode of atmospheric variability over the Atlantic sector. This finding implies a remote impact of the convective activity over the Indian Ocean on European Climate.

Interannual variability of diabatic heating during the Indian Summer Monsoon (ISM) drives a circumglobal teleconnection pattern in the northern hemisphere. This pattern in turn affects climate and rainfall in several regions of the world, especially in northeast China and northern Africa.

The results further suggest that teleconnection patterns associated with anomalous rainfall over the Tropical Indian Ocean, the Maritime Continent, the Indian peninsula and the Gulf Stream, bear similarities to the circumpolar wavetrain discussed in Branstator (2002).

In the tropics, the atmospheric response to diabatic heating resembles the Gill-type response, emphasizing that the satellite ensemble mean rainfall is a good representation of diabatic heating in the last 32 years.

Zusammenfassung

In dieser Arbeit werden atmosphärische Telekonnektionen auf ihre interannuelle Verbindung zu lokaler Niederschlagsvariabilität in den Sommern und Wintern nach 1979 untersucht. Wegen der Qualitätsprobleme von Reanalyseniederschlägen, insbesondere in der Zeit vor 1979, wird das Mittel aus drei unabhängigen satellitengestützten Niederschlagsprodukten berechnet. Dieses *Ensemblemittel* deckt 32 Jahre ab und wird als ein Proxy für diabatische Erwärmung in der Troposphäre verwendet. Es wird gezeigt, dass die diabatische Erwärmung, die bei starkem Niederschlag auftritt, die Zirkulation in der Troposphäre selbst in Regionen beeinflussen kann, die weit entfernt sind von der Region des erhöhten Niederschlages. Die dabei erzeugten Telekonnektionen können ihrerseits das globale Klima und Wetter beeinflussen. Planetare Wellen sind für die Generierung der Telekonnektionen verantwortlich, was durch eine Analyse der *Rossby Wave Source (RWS)* gezeigt wird, die Vorticity generiert. Dabei spielen die Strahlströme in mittleren Breiten eine wichtige Rolle bei der Erzeugung von Telekonnektionen, da sie als Wellenleiter für planetare Wellen fungieren.

Im tropischen Pazifik reproduziert der Niederschlag des Ensemblemittels sehr gut die Telekonnektionen, die mit El Niño assoziiert werden. Diese sind das Pacific North American (PNA) pattern und das Pacific South American (PSA) pattern.

Darüber hinaus wird gezeigt, dass selbst dann noch Regionen existieren, in denen erhöhter Niederschlag die globale Atmosphärenzirkulation antreibt, wenn das Signal von El Niño und das der lokalen Meeresoberflächentemperatur entfernt wird.

Im Winter projiziert erhöhter Niederschlag über dem tropischen Indischen Ozean auf die positive Phase der Nordatlantischen Oszillation (NAO), welche die dominante Mode der Klimavariabilität über dem Atlantischen Sektor ist. Dieses Ergebnis impliziert, dass Konvektionsaktivität über dem Indischen Ozean das Klima in Europa beeinflusst.

Interannuelle Variabilität in der diabatischen Atmosphärenerwärmung während des Indischen Sommermonsuns (ISM) erzeugt eine zirkumglobale Telekonnektion in der nördlichen Hemisphäre. Diese Telekonnektion übt wiederum einen signifikanten Einfluss auf das Klima und den Niederschlag in weiten Teilen der Welt aus, insbesondere im Nordosten Chinas und in Nordafrika.

Des Weiteren deuten die Ergebnisse darauf hin, dass die Telekonnektionen, die in Verbindung stehen mit erhöhtem Niederschlag über dem Indischen Ozean, dem Maritimen Kontinent, Indien und über dem Golfstrom, den zirkumpolaren Wellenzug widerspiegeln, der in Branstator (2002) diskutiert wird.

In den Tropen ähnelt die atmosphärische Antwort auf diabatische Erwärmung der *Gill-type response*. Dies untermauert, dass der saisonale Niederschlag des Ensemblemittels für die Zeit von 1980 - 2011 eine gute Repräsentation der diabatischen Erwärmung in der Troposphäre ist.

Contents

1. Introduction

In atmospheric sciences, the term *teleconnection* describes the tendency of atmospheric parameters, in most cases geopotential height, but also temperature or wind speed, to show similar behaviour between geographically widely separated points throughout the globe. Teleconnections are large - scale, simultaneous interrelations between geographical locations and they are usually active on time scales of a week up to a season (Wallace and Gutzler, 1981). Wallace and Gutzler (1981) associate teleconnections with standing oscillations in the troposphere geopotential height. They analyse one-point correlation maps of the fields of geopotential height to reveal geographically dependent, recurrent teleconnection patterns. Figure 1 shows their correlation maps for two base points [45°N, 165°W] and [55°N, 20°W], obtained using the 45 winter months (DJF) from 1962/63 to 1976/77. One can clearly identify patterns consisting of well-separated patches of different amplitude. Wallace and Gutzler (1981) name these particular patterns the Pacific North American (PNA) pattern (top panel) and the East Atlantic (EA) pattern (lower panel). Another way to find dominant patterns of low frequency variability in the atmospheric circulation is to carry out an Empirical Orthogonal Function analysis (EOF, see von Storch and Zwiers (1999) for details). EOFs of sea level pressure (SLP) or geopotential height at a certain pressure level are used in many studies to detect circulation regimes in a domain of interest (Mo and Peagle, 2001, Hurrell et al., 2003, Sun et al., 2010, amongst many others). Several examples of prominent teleconnection patterns, including those which will be mentioned in this thesis, are described and defined in section 2.5.

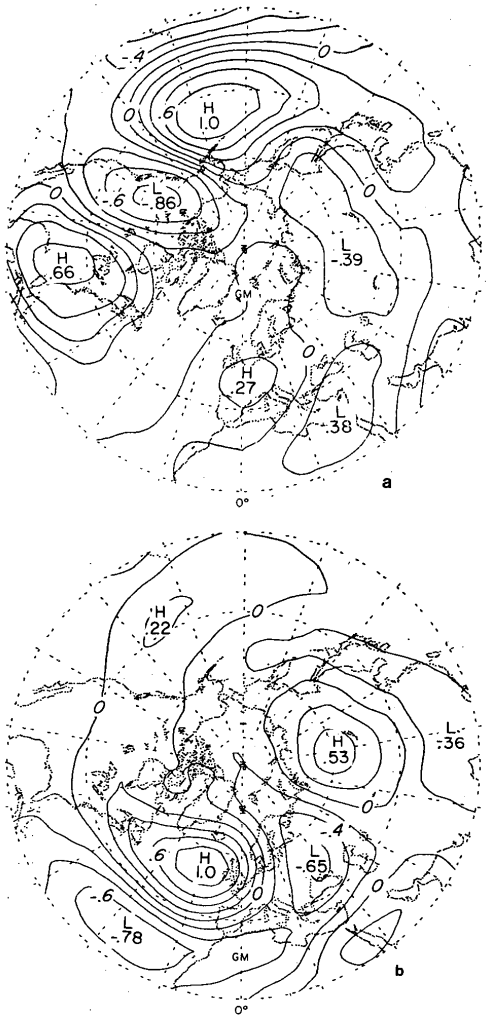

Figure 1: DJF monthly mean one-point correlation of 500 hPa geopotential height at the grid points a) 45°N, 165°W, b) 55°N, 20°W. Contour interval is 0.2. a) closely resembles the PNA pattern, b) the EA pattern (from Wallace and Gutzler (1981)).

Teleconnections are of large scientific and socio-economic interest since the variability of the atmospheric circulation associated with teleconnections is known to affect the weather in many regions of the world. For example, winter rainfall in Western Europe and Scandinavia is strongly dependent on the state of the North Atlantic Oscillation (NAO), since it determines the strength of the midlatitude westerly winds across Europe that advect moist marine air masses from the Atlantic (Greatbatch, 2000, Hurrell et al., 2003).

Another example demonstrating how atmospheric circulation can affect local rainfall is given by Mo and Peagle (2001), who point out the role of the Pacific-South American (PSA) pattern in modulating rainfall over South America. This motivates the investigation of what drives such low frequency (interannual), recurrent atmospheric teleconnection patterns. Are they purely internal variability in the climate system arising from eddy-mean flow interaction, or may they be excited by a local forcing of the atmosphere, such as enhanced diabatic heating, which occurs in times of excessive rainfall and thus anomalous deep convection? Nowadays, it is widely believed that many prominent teleconnections appear as the atmospheric response to deep convection caused by the slowly varying tropical SSTs (Trenberth et al., 1998), but one must note that there may also be regions where strong convective activity is found, that can drive the atmosphere without being necessarily related to the underlying SST. Using observational data alone, one is limited in detecting and distinguishing between different driving mechanisms for the atmosphere. Thus, there are many studies analysing the atmospheric response to an imposed local forcing using General Circulation Models [GCMs, (e.g. Hoskins and Karoly, 1981)] or simple vorticity balance models (Sardeshmukh and Hoskins, 1988). Hoskins and Karoly (1981), for example, point out that a linear baroclinic model of the atmosphere can exert global scale wave trains for both thermal and orographic forcing.

While most classical studies used SST anomalies as forcing, nowadays it has also proven equally effective to integrate the model with a specified general tropical heating source centred at a certain (tropospheric) level (Hoskins and Karoly, 1981, Sun et al., 2010, Greatbatch et al., 2013). Local sources of diabatic heating are shown to initiate global scale teleconnections (e.g. Hoskins and Karoly, 1981, Sardeshmukh and Hoskins, 1988, Lin, 2009). In the real world, these sources may be associated with strong local rainfall events, persisting sometimes over several months.

The general complication concerning the dynamical connection between rainfall and atmospheric

circulation can nicely be illustrated when thinking again about the aforementioned PSA pattern and its correspondence to El Niño Southern Oscillation (ENSO). ENSO is a complex ocean - atmosphere coupled phenomenon, that involves both SST anomalies along the central to eastern tropical Pacific and anomalous vertical motion in the Pacific domain. While assumed to affect South American rainfall via advection of moist air, the PSA pattern itself is thought to be the atmospheric response to ENSO in the Southern Hemisphere (Mo and Peagle, 2001), given the anomalous deep convection and rainfall in the eastern tropical Pacific during strong ENSO events. To give an example for boreal summer, Greatbatch et al. (2013) suggest a dynamical response of the atmosphere to excessive rainfall in India during the Indian summer monsoon (ISM). This response in turn projects onto the second mode of variability of the wind field in an enclosed region over China, such that the atmospheric response finally leads to enhanced rainfall over northern China (Sun et al., 2010). Further, Ding and Wang (2005) point out that the ISM heating provides a possible forcing mechanism for a circumglobal teleconnection pattern, which in turn significantly affects rainfall in parts of Western Europe, Russia, North America and Asia. These examples demonstrate general difficulties in distinguishing, on an interannual basis, whether it is the atmosphere that drives the rainfall, or vice versa. Thus, understanding the associated relationships and causalities may yield improvements in predictability of climate in many regions of the world.

Hence, there are numerous studies to explain possible mechanisms for how a local forcing, like deep convection due to anomalous surface heating or latent heat release by anomalous rainfall, can induce atmospheric circulation changes. Using 3-hourly radiosonde data, Mitovski and Folkins (2014) show that during the 1-2 days period around a strong rainfall event, the troposphere near the rainfall region is significantly affected. In particular, positive geopotential height- and temperature anomalies are observed in the mid to upper troposphere (400 - 200 hPa), while negative geopotential height- and temperature anomalies prevail at lower levels. Mitovski and Folkins (2014) find these effects in the troposphere to extend 600-1000 km radially away from the location of the strong rainfall event.

Trenberth et al. (1998) point out the role of tropical surface forcing in producing tropical deep convection, which in turn strengthens the Walker- and Hadley circulation. In upper tropospheric levels this results in anomalous divergence of the meridional wind in the tropics and anomalous convergence at higher latitudes. Finally, these anomalies can act as a Rossby wave source and thus initiate the overall atmospheric response, even at latitudes far away from the forcing region (Sardeshmukh and Hoskins, 1988). They further claim that the longitudinal position of the tropical

heating is essential to the actual response pattern, such that there exist some preferred pathways for teleconnective responses in the tropics.

The theoretical basis for the forcing of planetary waves in the tropics has its beginnings in the work of Matsuno (1970) and Gill (1980). Condensing the most important points from these studies, the tropical response is governed by a fast Kelvin wave to the east of the forcing region and a slower Rossby wave response to the west. The equatorial Kelvin wave travels eastward, leaving anomalous low pressure in its wake at the surface and anomalous high pressure aloft. According to Gill (1980), the footprint of the slower westward propagating Rossby wave at the surface is given by two cyclones (anticyclones aloft), that are symmetric about the equator and are located slightly north- and south west of the forcing region. On the other hand side, for a response to penetrate out of the tropics, the overall existence of subtropical Rossby waves is crucial and therefore, generation of a Rossby wave source in the subtropics is favourably (Sardeshmukh and Hoskins, 1988). Further, the response in high latitudes becomes more and more barotropic, while in the Tropics, the response is rather baroclinic.

In the pioneering work of Wallace and Gutzler (1981) on teleconnections, there were only 15 years of geopotential height data available, which raises the question about reproducibility and stationarity of the teleconnections on longer time scales. The aim of this thesis is to further consolidate and examine atmospheric teleconnection patterns and their relation to local rainfall anomalies. Therefore, an ensemble of three satellite rainfall products for the last 32 years is used to investigate the effect of rainfall on the atmosphere. To our knowledge, this particular analysis has not been undertaken before.

The launch of rainfall measuring satellites in the 1970s greatly enhanced the quality of precipitation data, especially over the oceans, and enabled their availability as global gridded data (Arkin and Meisner, 1987, Efthymiadis et al., 2005). One must keep in mind that prior to the satellite era, observational precipitation data were restricted to land-based rain gauges and ship cruise measurements, both suffering temporal and spatial inhomogeneity.

The questionable quality of (tropical) rainfall in reanalysis data, especially in the pre - satellite era, is discussed, for example, in Poccard et al. (2000) and Efthymiadis et al. (2005). In Figure 2, local rainfall estimates of two reanalysis products (NCEP/NCAR and ERA40) are compared with CMAP satellite measured rainfall. It clearly depicts the discrepancies between reanalysis and

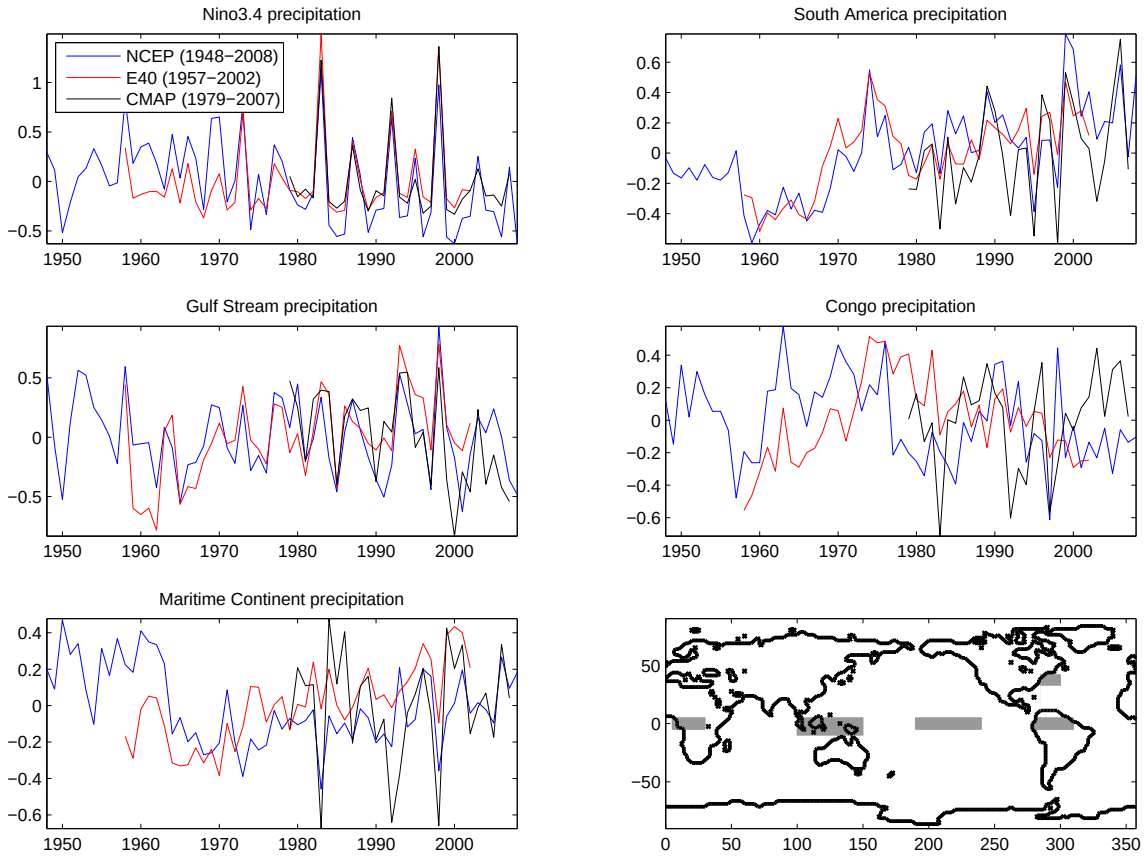

Figure 2: Some examples of normalized DJF mean rainfall anomalies for five regions of the world (see section 2 for details about the rainfall data and rainfall regions). Shown are the values from both reanalysis NCEP (blue) and ERA40 (red), as well as CMAP satellite rainfall anomalies (black). Bottom right shows the position of the boxes.

CMAP in the satellite era, but also the discrepancies between the two reanalysis products in the pre- satellite era, especially in the tropics. There have been attempts to reconstruct pre - 1979 oceanic precipitation using land-based gauge data or reanalysis precipitation (Efthymiadis et al., 2005). The authors, however, find that the reconstruction skill is poor in regions far away from the coast and in years without ENSO activity. Since we are also interested in processes apart from ENSO, we decided to focus our study on rainfall data derived from satellite soundings (period after November 1979) and investigate their effect on the atmosphere. Thus, the data analysed here span a time of well above 30 years, which allows for confidence in the results, when using typical statistical time series analysis methods to examine the relationship between local rainfall and teleconnections.

2. Data and methods

2.1. Rainfall data

Given the large discrepancies regarding tropical rainfall amongst different rainfall products (Figure 2), this study uses different satellite-based rainfall products, although this restricts the analysis to the period after 1979. This is reasonable, because the quality of NCEP/NCAR rainfall has been found to be very questionable in the pre-satellite era (Poccard et al., 2000, for example). On the other hand, the availability of satellite rainfall sensors, which operate at microwave and infra-red wavelengths, has dramatically improved both accuracy and spatial homogeneity of global rainfall data (see, for example, Arkin and Meisner, 1987, Todd and Washington, 1999).

Our aim is to average different rainfall products in the regions sketched in Figure 4 in order to generate an *ensemble mean* rainfall. We decided to use an ensemble of three independent satellite based rainfall data sets, which will be introduced in the following. One product is the Global Precipitation Climatology Project [GPCP, Adler et al. (2003)], which combines monthly satellite data with estimates from over 6,000 rain gauge stations, low-orbit infrared, passive microwave, and sounding observations. This provides a very complete analysis over the World Oceans, and adds additional information over land to increase accuracy. Data are available from 1979 to present at a spatial resolution of 2.5°. The second product used is CPC Merged Analysis of Precipitation [CMAP, Xie and Arkin (1997)], which contains monthly data from five kinds of satellite estimates (GPI,OPI,SSM/I scattering, SSM/I emission and MSU). Data are available from 1979 to present and are stored at 2.5°horizontal resolution. The third product used here is the Climate Anomaly Monitoring System (CAMS) and OLR Precipitation Index (OPI); see, for example, Janowiak and Xie (1999). This analysis combines OPI satellite rainfall estimates with data from rain gauges (CAMS) to get real-time monthly estimates of global precipitation on a 2.5°x 2.5°grid from 1979 to present. The term *ensemble mean*, which is used in this study, refers to the mean of the GPCP, CMAP and CAMS/OPI precipitation.

Regarding the analysis of summertime rainfall, an additional rainfall product is used for the Indian region: the All India Rainfall Index (Parthasarathy et al., 1995). This dataset has the advantage of yielding uninterrupted rain gauge data from 2000 back to the year 1871. This enables a comparison with atmospheric parameters from the early NCEP/NCAR reanalysis (post 1949). The dataset contains annual estimates for the cumulative June/July/August/September (JJAS) rainfall, taken

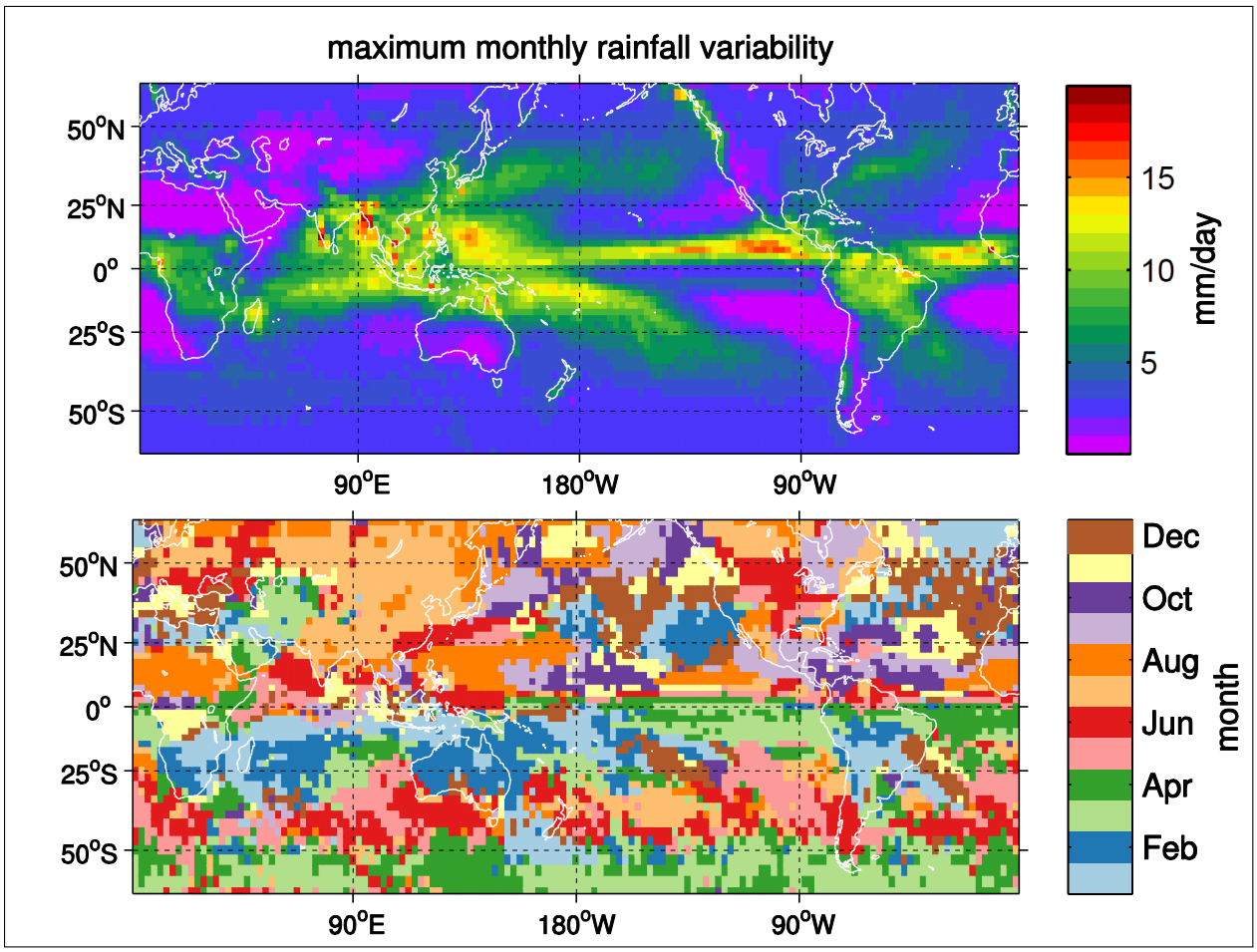

Figure 3: Maximum monthly mean rainfall variability. Shown is the highest standard deviation of the interannual monthly mean rainfall variability (top) and the corresponding month of the occurrence of this maximum standard deviation (bottom)

from 306 stations in India. The authors claim that the number and distribution of rain gauges is consistent until 1990, but the number and distribution of rain gauges is unknown from 1991 - 2000.

2.2. General rainfall analysis

Figure 3 shows the maximum standard deviation of the interannual variability of monthly mean rainfall and the month of occurrence of the maximum in this standard deviation. The ensemble mean rainfall is used here. According to the map, several geographical boxes are chosen, where strong variability is found in the boreal winter time: The Central Pacific region (CP), the Maritime Continent (MC), The Gulf Stream (GU), the Tropical Indian Ocean (IO), the Tropical Eastern Pacific Nino region (Nino3.4 box) and the South America (SA) box. There are also regions where rainfall variability peaks in boreal summer. For this study, the regions of India (IND), Northern China (CH) and the Sahel are of particular interest. The exact geographical locations of these boxes are summed up in Table 1 and in Figure 4, respectively. A special case is the Congo (CO) box, where variability peaks in October/November, but further analysis (Figure 5) shows that the

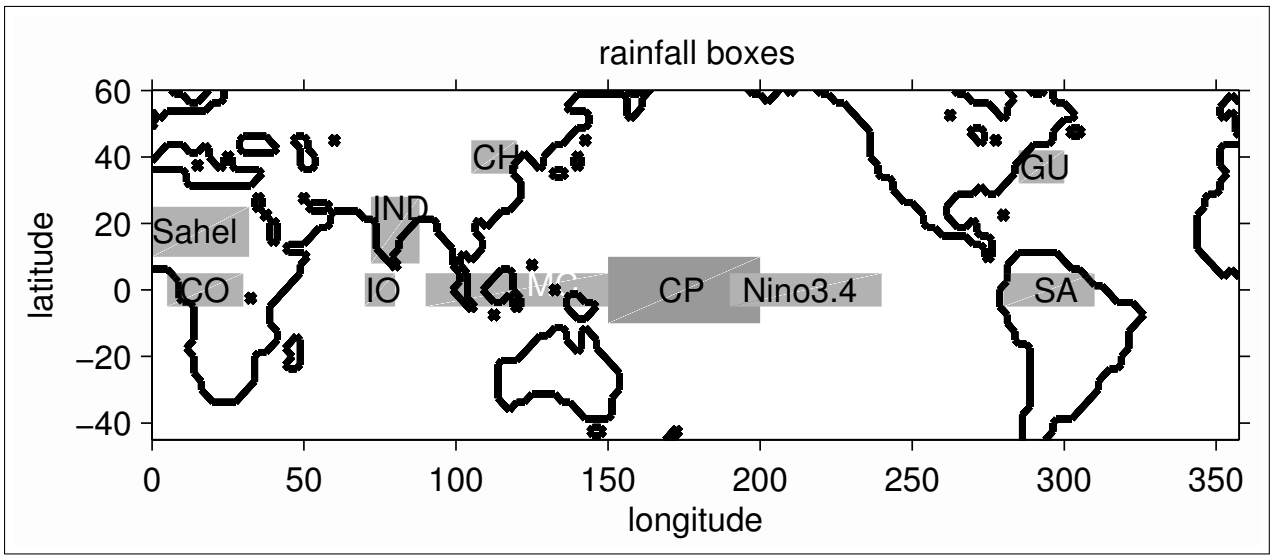

Figure 4: Map showing the location of the boxes listed in Table 1.

seasonal cycle is dominated by a double-peak structure in boreal spring and autumn, which is very likely the manifestation of the Intertropical Convergence Zone (ITCZ), that crosses the equator twice a year and is associated with enhanced rainfall. The seasonal cycle of precipitation in these boxes, as well as its variability, is shown in Figure 5. It reveals regions of comparably low variability throughout the year (the three summer boxes IND, CH, Sahel, and IO) and regions with a strong seasonal cycle in terms of rainfall variability (e.g. Nino3.4, MC, CP). From Figure 5, it seems that strongest amounts of rainfall are likely to coincide with the month of strongest rainfall *variability*. One exception from that is the Nino3.4 box, where maximum rainfall occurs in boreal spring (MAM), while strongest variability is found in boreal winter (DJF). We thus conclude to restrict our analysis to DJF mean rainfall for the winter boxes and JJAS mean rainfall for the summer boxes (JJAS for enabling comparison with All India Rainfall Index).

Box	**°lat**	**°lon**
Nino3.4	5S - 5N	190E - 240E
CP	10S - 10N	150E - 200E
MC	10S - 5N	100E - 150E
GU	32N - 42N	285E - 300E
IO	5S - 5N	70E - 80E
CO	5S - 5N	5E - 30E
IND	8N - 28N	72E - 88E
CH	35N - 45N	105E - 120E
Sahel	10N - 25N	358E - 32E

Table 1: Geographical position of the rainfall boxes which are considered in winter (top) or summer (bottom), for the longitudinal and latitudinal limits, the first number is the westernmost (southernmost) limit for each box

Accordingly, Figure 6 shows time series of DJF and JJAS rainfall, averaged in the correspond-

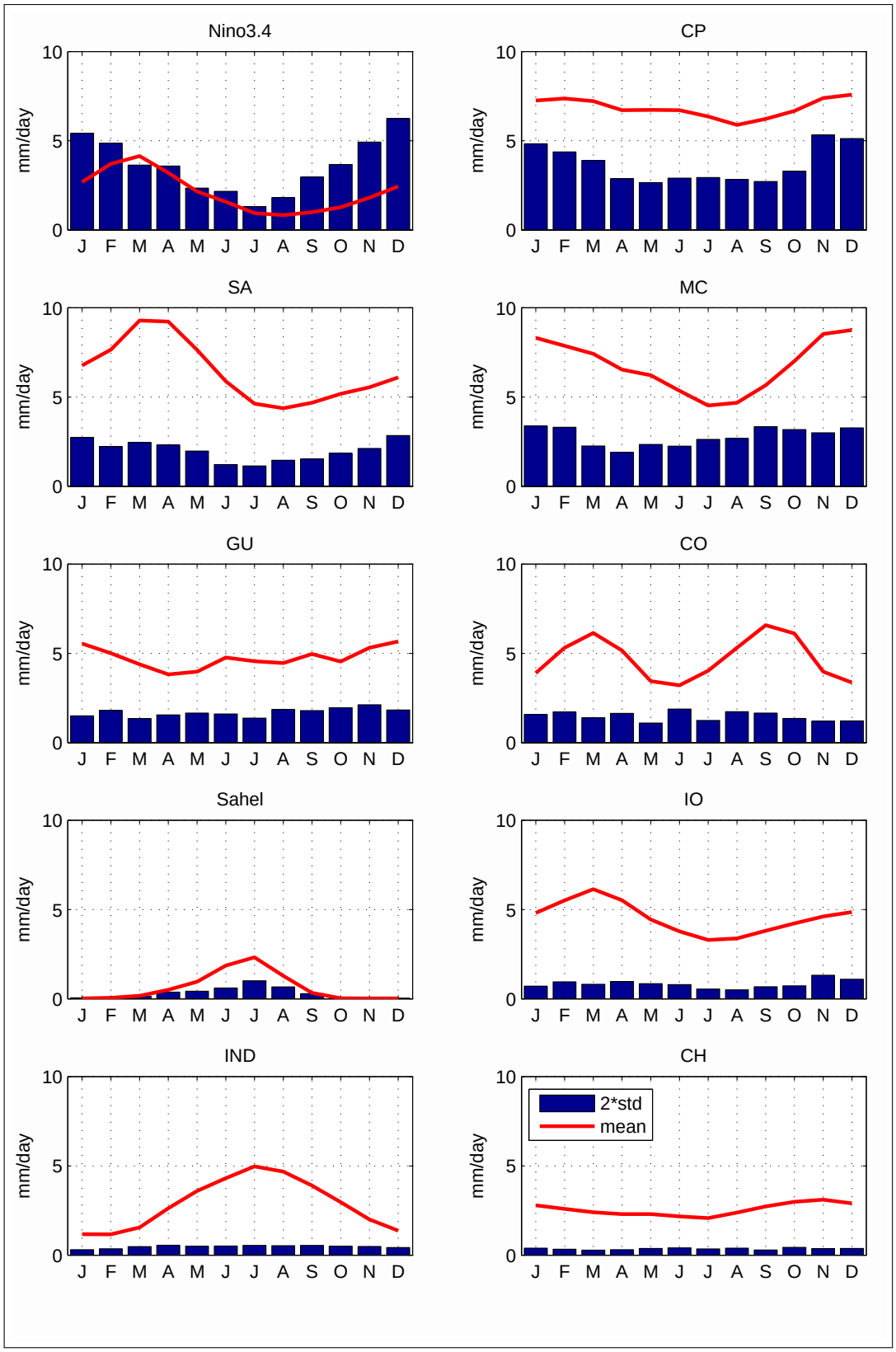

Figure 5: Seasonal cycle (red curves) and 2 · standard deviation (blue bars) of interannual monthly mean precipitation (seasonal cycle removed) in rainfall boxes using the satellite ensemble mean product from 1979-2011

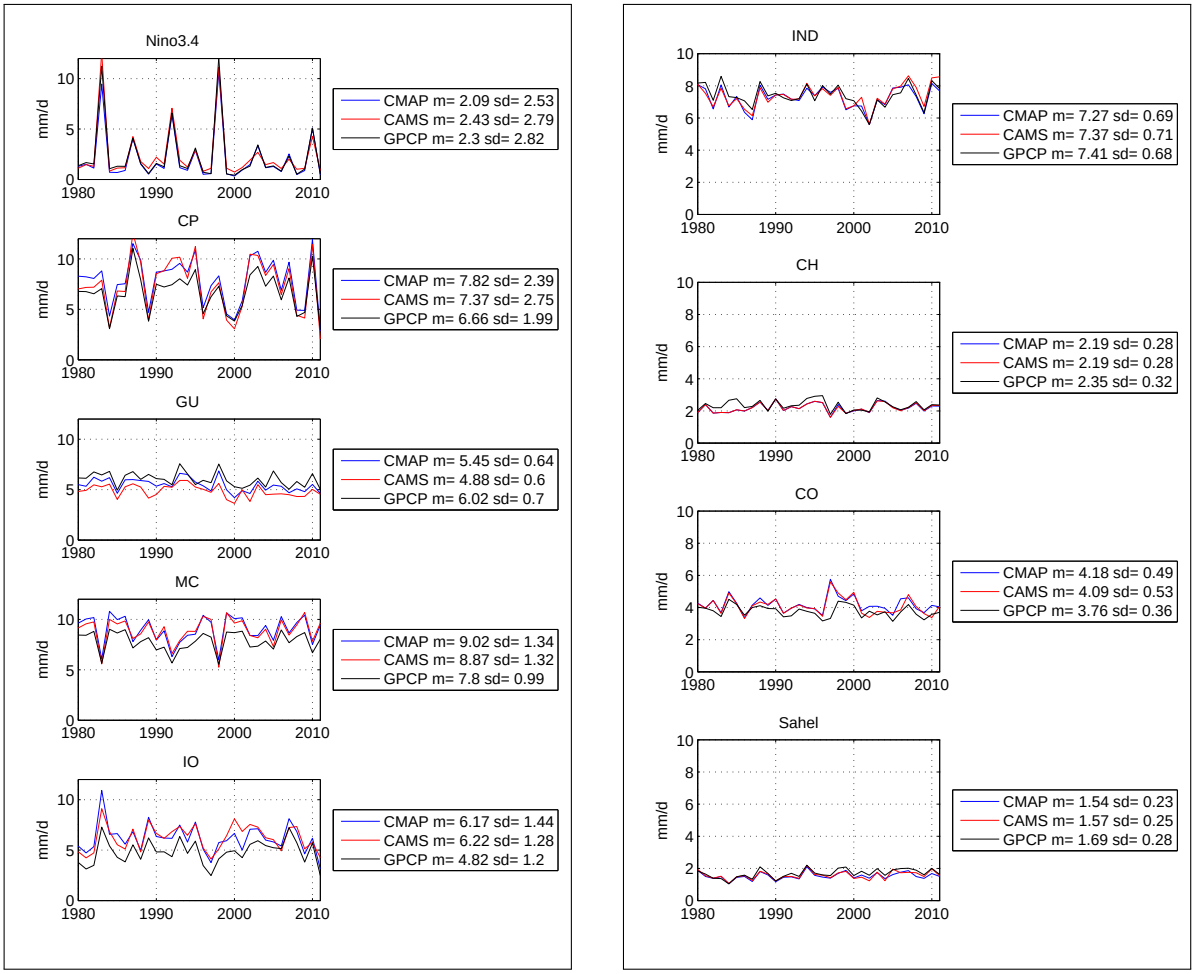

Figure 6: DJF (left) and JJAS (right) rainfall estimates for the boxes listed in Table 1. Mean and standard deviation for each product are given in the legend.

ing geographical boxes. The averaging has been constructed as an area average. This means that data were weighted by the cosine of latitude to account for the changes in the area of a grid box with latitude. Finally, the data were divided by the sum of the weights. One can see the robustness of precipitation in the winter time Niño3.4 region, as well as the footprint of the ENSO signal on most of the other winter time series. There are remarkable qualitative and quantitative similarities between the three rainfall products, which further motivates the use of an ensemble mean rainfall. Figure 7 provides a general comparison of the three satellite rainfall products used to build the ensemble. It can be seen in a) - c) that CMAP, CAMS/OPI and GPCP agree well with each other almost everywhere in both the tropics and extratropics. This is indicated by correlation coefficients of > 0.6 almost everywhere. In particular, the three products are highly correlated ($r > 0.9$) over the tropical oceans, as well as over most parts of the continents. The correlations are lower over the subtropical and especially over the subpolar oceans. In these regions, DJF mean rainfall is, at the 95% confidence level, locally not even significantly correlated amongst the three rainfall products. Continental regions where the three products do not agree well are Africa, Arabia and

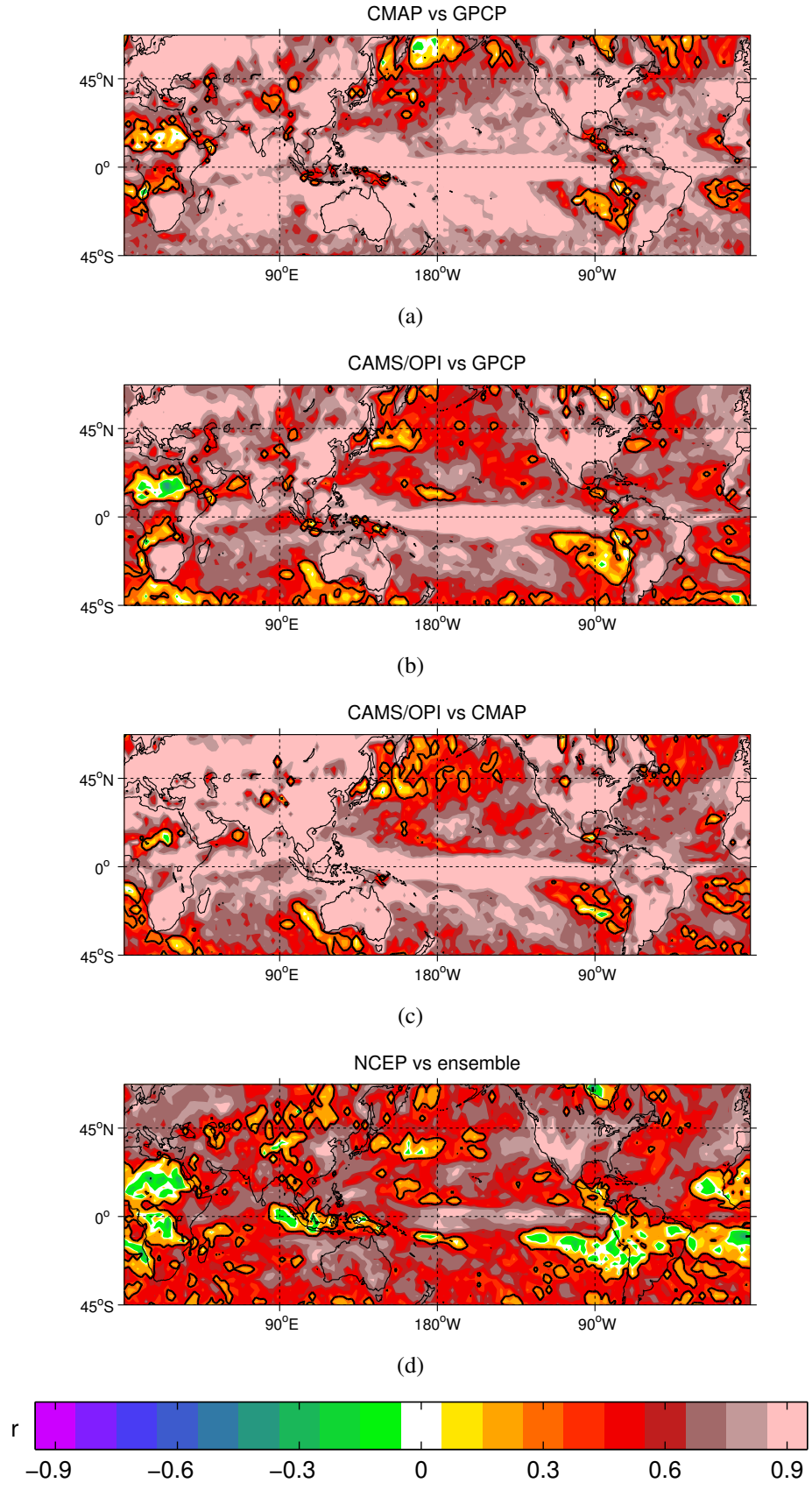

Figure 7: DJF winter mean local correlation coefficient between a) CMAP and GPCP, b) CAMS/OPI and GPCP, c) CAMS/OPI and CMAP, d) NCEP/NCAR and the satellite ensemble mean rainfall. Note that NCEP/NCAR rainfall is not used to calculate the ensemble mean. Colour contouring in steps of 0.1. Black line shows the 95% confidence level of the correlation ($r_{crit} \approx \pm 0.35$). Time series have been detrended.

the south-eastern vicinities of the Atlantic and Pacific oceans. When comparing this with figure 3 a), one finds that those regions where the three satellite based rainfall products differ most strongly from each other, are regions of very weak rainfall variability. These regions are namely the Sahara, Arabia and the Subtropical eastern ocean basins, where maximum monthly rainfall standard deviation barely exceeds 1 mm/day. In Figure 7 d), the correlation of the ensemble mean rainfall with the NCEP rainfall is provided. Although NCEP rainfall is not included in our ensemble mean rainfall, it is striking that the correlations are overall substantial weaker than for any of the satellite based products [a) - c)]. In the regions of the Maritime Continent, Congo and South America, for example, the correlation with the satellite ensemble is mostly smaller than 0.3 and not significant. Even in the tropical Pacific region, where the satellite products agree well with each other, correlation coefficients of only 0.6 - 0.8 are found. This illustrates the reason for not using DJF NCEP rainfall in our analysis.

Throughout this study, statistical significance of correlations and regressions is calculated using the p-value of a test statistic (two-sided students t-test), where the Null Hypothesis is that the true Pearson correlation coefficient is zero. In all cases, the time series have been detrended. Before computing the correlation coefficient, it is assumed that each year is independent of the other. The number of degrees of freedom equals the number of winters (summers) making up the time series.

Regarding the winter time, a strong correlation between most of the time series is found, especially in the Pacific sector (see Table 2). For completeness, Figure 8 shows the impact of ENSO on the local rainfall in most parts of the world. These results demonstrate the strong impact of ENSO, even in regions far away from the Nino3.4 box. In order to extract variability in rainfall which is not due to ENSO, the linear effect of the Nino3.4 rainfall signal is removed from each

	Nino3.4	**CP**	**SA**	**GU**	**MC**	**IO**
Nino3.4	1	0.38	-0.57	0.39	-0.85	0.35
CP	0.38	1	-0.68	0.36	-0.62	n.s.
SA	-0.57	-0.68	1	n.s.	0.69	n.s.
GU	0.39	0.36	n.s.	1	-0.46	n.s.
MC	-0.85	-0.62	0.69	-0.46	1	-0.42
IO	0.35	n.s.	n.s.	n.s.	-0.42	1

	IND	**CH**	**Sahel**
IND	1	n.s.	0.56
CH	n.s.	1	n.s.
Sahel	0.56	n.s.	1

Table 2: Correlation coefficients of DJF (left) and JJAS (right) rainfall time series, "n.s." means correlation is not significant the 95% confidence level ($r_{crit} \approx \pm 0.35$)

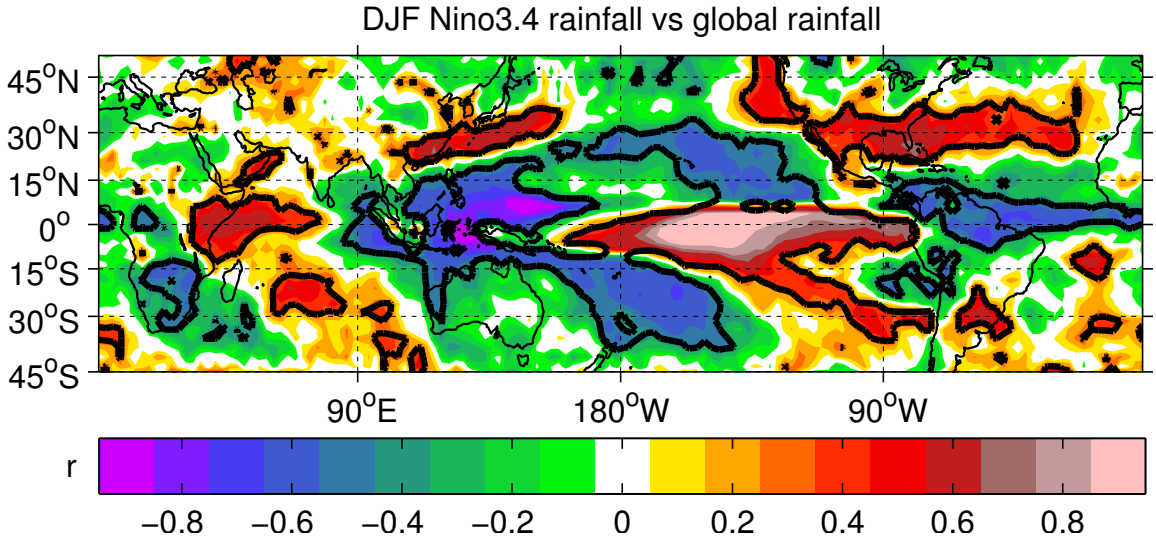

Figure 8: Correlation coefficient of DJF Nino3.4 rainfall with global rainfall. Colour contouring in steps of 0.1. 95% confidence interval of the correlation is indicated by the black line. Critical correlation coefficient is $\approx \pm 0.35$. Time series have been detrended.

time series. The procedure is described in the next section. In summer (JJAS), the only correlation that is significant at the 95% confidence level is found between India and Sahel (r = 0.56). This link is well known and documented in the observational and modelling climate community (see, for example, Kraus (1977), Ward (1998), Raicich et al. (2003), Zhang and Delworth (2006)) and will be picked up later.

In the JJAS analysis, there is no significant correlation found between India and Northern China. However, in the community, this link is a topic of discussion (Sun et al., 2010, Greatbatch et al., 2013, for example) and will be further examined later.

2.3. Removing the ENSO signal

In the last section we showed that the footprint of Nino3.4 rainfall is found in most of the rainfall time series in the winter. Figure 8 provides evidence that in the winter season, interannual rainfall variability over many parts of the tropical and subtropical oceans and continents is related to the interannual variability of ENSO. A summary of rainfall patterns that are associated with ENSO is given, for example, in Ropelewski and Halpert (1987). In order to isolate the non - ENSO related rainfall signal, a regression analysis is carried out to remove the Nino3.4 rainfall signal from all the time series on the grid, such that the correlation coefficient between any rainfall time series and the Nino3.4 rainfall is zero. In other words, from each time series the part is subtracted which is linearly congruent with the Nino3.4 signal. The regression is done to the DJF and JJAS anomalies,

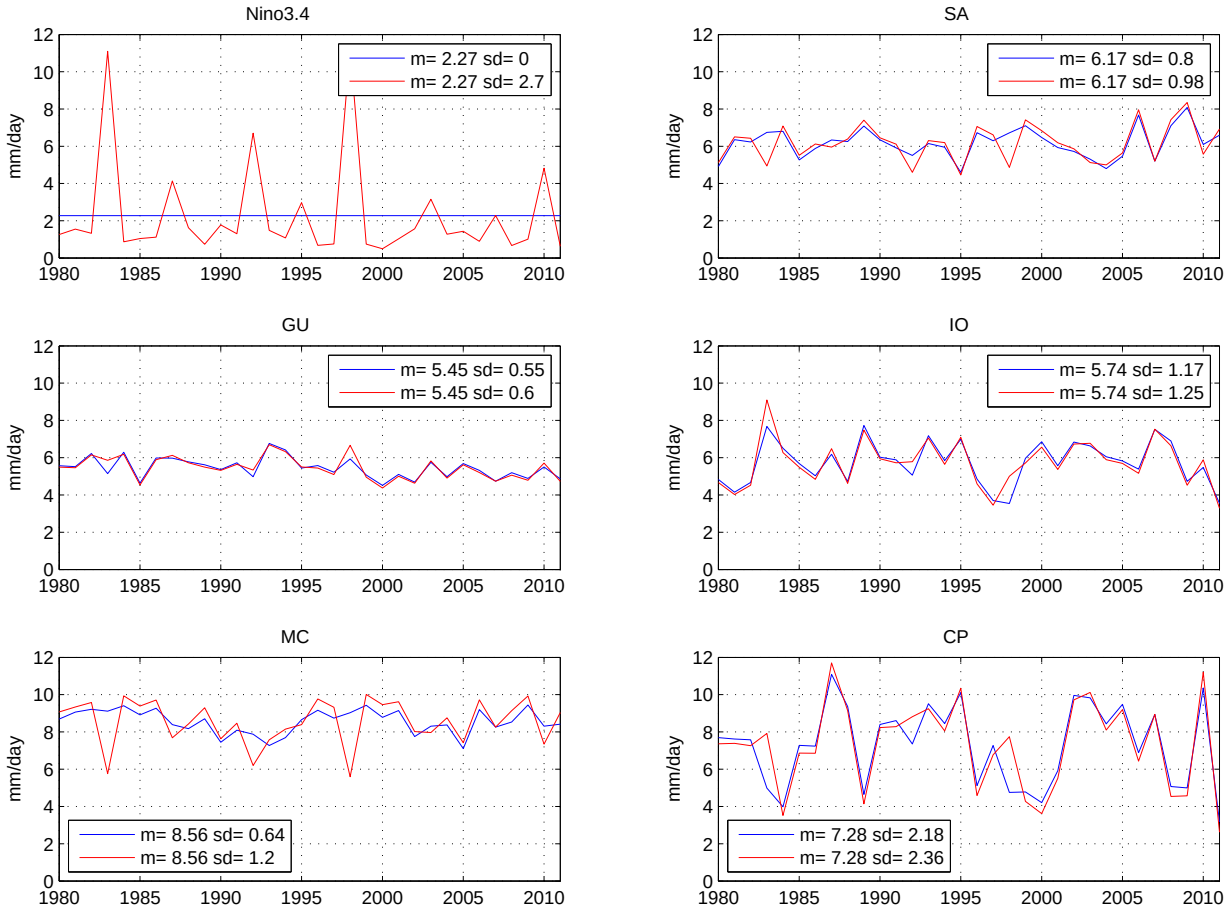

Figure 9: DJF mean rainfall estimates including (red) and excluding (blue) the Nino3.4 rainfall signal for the rainfall boxes in Table 1 and Figure 4. Note the mean stays constant.

while the original mean precipitation for each box is added back. This technique ensures that the mean rainfall at each site stays untouched, while the Nino3.4 signal gets removed. The corresponding rainfall time series are shown in Figure 9. Given the change in the standard deviations between the blue and the rad curves in Figure 9, it also becomes obvious that a significant fraction of variability is removed from the time series, especially for the MC rainfall. Note the strong El Niños of 1983, 1992 and 1997 are not evident anymore in the corrected time series. However, even after removing the effect of Nino3.4 rainfall from the other time series, one can see there is still remarkable coherence over the tropical Pacific region (see Table 3), with SA rainfall being in opposite phase to CP and in phase with MC rainfall. We note that throughout

	CP	**SA**	**GU**	**MC**	**IO**
CP	1	-0.61	n.s.	-0.62	n.s.
SA	-0.61	1	n.s.	0.47	n.s.
GU	n.s.	n.s.	1	n.s.	n.s.
MC	-0.62	0.47	n.s.	1	n.s.
IO	n.s.	n.s.	n.s.	n.s.	1

Table 3: Correlation coefficients of DJF rainfall time series without the ENSO signal, "n.s." means correlation is not significant the 95% confidence level. The corresponding time series are shown in Figure 9.

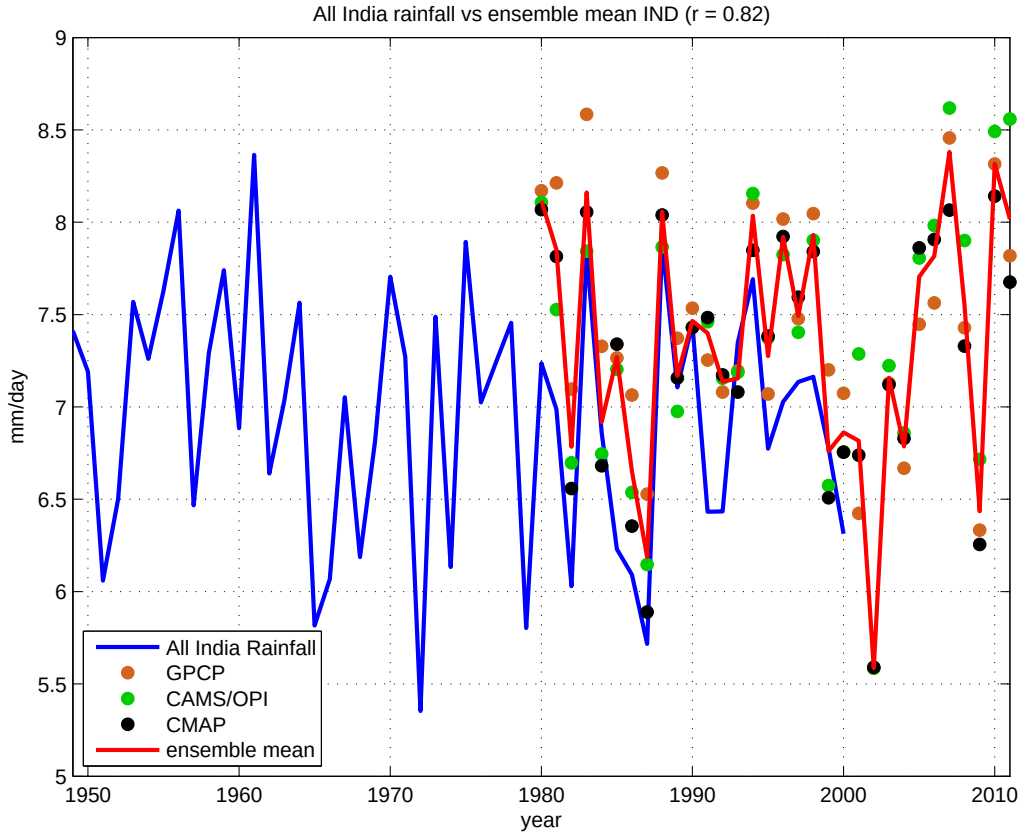

Figure 10: All India JJAS rainfall time series (blue), JJAS satellite products (dots) and JJAS ensemble mean rainfall (red). ENSO is removed. Correlation coefficient between the blue and the red curve is 0.82 in the period of overlap.

the remainder of this thesis, Nino3.4 rainfall has been systematically removed from any rainfall time series that is discussed, even for those in summer and from those which are not significantly correlated with Nino3.4 rainfall.

Figure 10 shows time series of All India rainfall together with the satellite estimates for the India box. In their overlapping time period, the satellite ensemble and All India rainfall are correlated at 0.82. Given the different spatial resolutions and inhomogeneity of the data, this is a surprisingly high value.

2.4. Atmospheric variables

We use monthly mean, gridded NCEP/NCAR data (Kalnay et al., 1996) for wind field, stream-function, geopotential height and sea level pressure. Geopotential height and wind field data are available on pressure levels on a 2.5°x 2.5°spatial grid from 1948 to present. Streamfunction is available as spectral model output (T62) from the NCEP/NCAR reanalysis, with an approximate spatial resolution of 1.875 °and a sigma coordinate as the vertical variable.

2.5. Documented recurrent teleconnection patterns

Wallace and Gutzler (1981) find five dominant teleconnection patterns in the monthly mean wintertime northern hemisphere circulation. When analysing atmospheric teleconnections, most studies concentrate on the boreal winter, since low frequency variability is most pronounced in that season (Blackmon, 1976). In this section, we will introduce the most prominent teleconnection patterns in DJF mean data. One is the *East Atlantic (EA)* pattern, which is defined by three centers: one south west of the Canary Islands (25°N, 25°W) , one near the Black Sea (50°N, 40°W), and a third, oppositely-phased center west of Great Britain (55°N, 20°W). The index of the EA pattern is then given by

$$EA = 0.5 \cdot Z(55°N, 20°W) - 0.25 \cdot Z(25°N, 25°W) - 0.25 \cdot Z(50°N, 40°E)$$

As in Wallace and Gutzler (1981), Z is the normalized anomalous 500hPa geopotential.

The *North Atlantic Oscillation (NAO)* was first described by Walker and Bliss (1932), who used normalized anomalous DJF temperature and pressure to yield:

$$NAO = P_{Vienna} + T_{Bodö} + T_{Stornoway} + 0.7 \cdot P_{Bermuda} - P_{Stykkisholm} \\ - P_{Ivigtut} - 0.7 \cdot T_{Godthaab} + 0.7 \cdot (T_{Hatteras} + T_{Washington})/2$$

According to this, a positive NAO index goes along with a stronger than usual Icelandic low, strong westerlies along the North Atlantic and higher than usual pressure at the Azores and in the Mediterranean at about 40°N. Using this general feature of the traditional NAO index from Walker and Bliss (1932), many authors simply construct their NAO index based on the surface pressure difference between the Azores and The Greenland/Iceland region, in order to avoid using as much as nine different inputs (e.g. Hurrell, 1995).

At this point, one general problem becomes obvious, which was already stressed by Wallace and Gutzler (1981) and, for the special case of the NAO, by Hurrell et al. (2003). It is difficult to establish one unambiguous definition for a certain teleconnection pattern, which often complicates the direct comparison with other studies that use different analysis.

In this study, however, we compute the NAO following Hurrell et al. (2003) as the first EOF of DJF

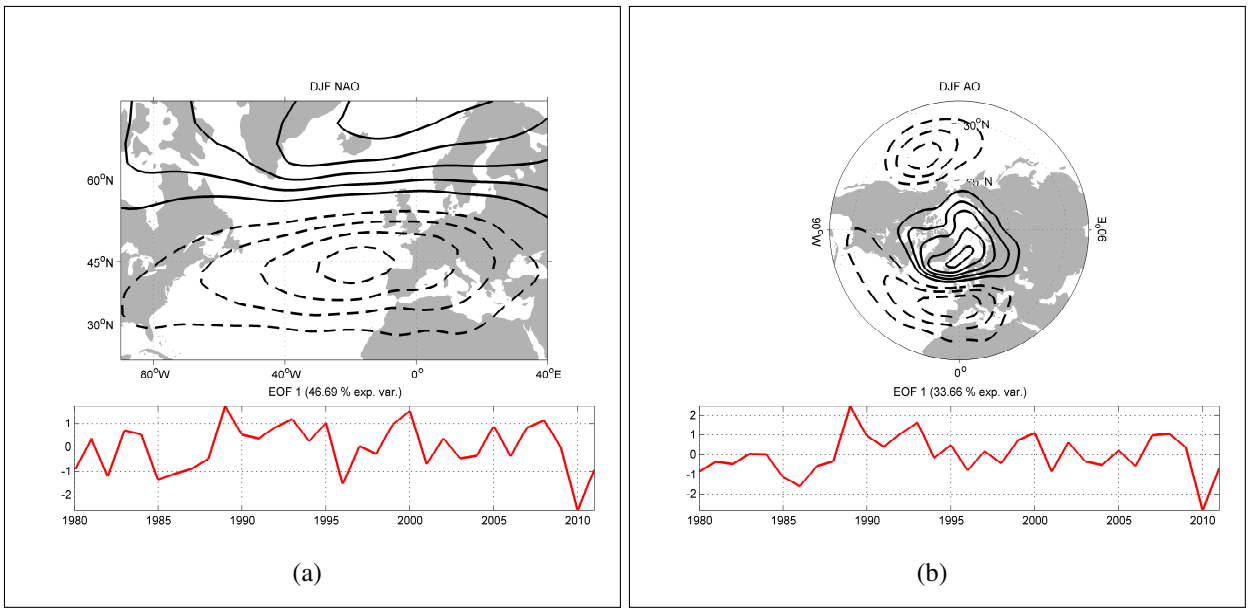

Figure 11: (a) NAO and (b) AO patterns and PC time series for the EOF-based definition of the NAO and AO. Contour interval is 8 gpm, negative values are dashed. Zero line is not plotted.

winter mean Z850 in the region 90°W - 40°E, 20°- 70°N, and the NAO index is then given by the PC series of this first EOF. This definition is rather natural, since it considers the Atlantic domain without any further assumptions about the shape of the NAO pattern. While the NAO considers the Atlantic domain of the northern hemisphere, one may also introduce the Northern Annular Mode (NAM), also called Arctic Oscillation (AO), obtained as the first EOF over the whole northern hemisphere north of 20°N (Hurrell et al., 2003). Both the NAO and AO patterns are shown in Figure 11. It is obvious that the NAO and AO are not independent from each other. In fact, their PC series are correlated at 0.91.

The *Pacific North American (PNA)* pattern consists of four equally weighted centers: One over Hawaii (20°N, 160°W), one over Alberta (55°N, 115°W), one over the North Pacific Ocean (45°N, 165°W), and one close to the Gulf region of the USA (30°N, 85°W), with the latter two centers being opposite in phase to the former two. The mathematical expression is

$$PNA = 0.25 \cdot [Z(20°N, 160°W) - Z(45°N, 165°W) + Z(55°N, 115°W) - Z(30°N, 85°W)]$$

The PNA and EA patterns are shown in Figure 1, as found by Wallace and Gutzler (1981).

Another pattern is the *Scandinavia pattern*, which was first discovered by Barnston and Livezey (1987) and given the name *Eurasian Pattern Type 1 (EU1)*. It has one center over Scandinavia between 60-70°N, 25-50°E, one oppositely phased center over North west China between 30-45°N,

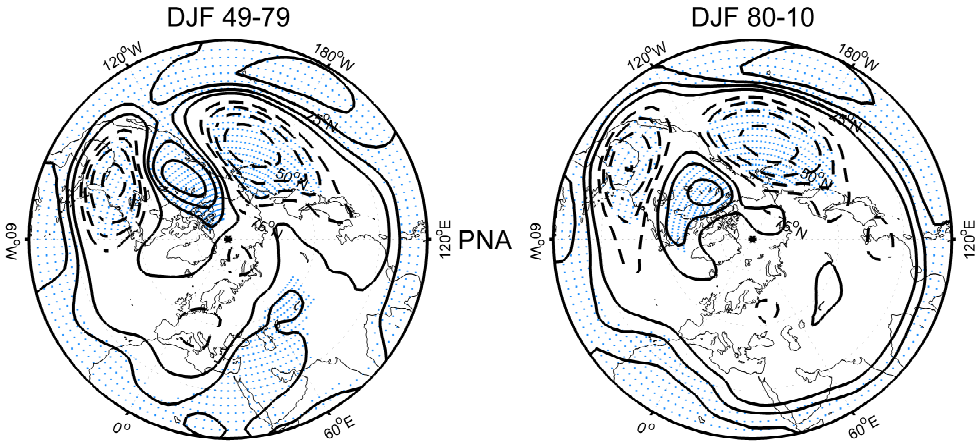

(a)

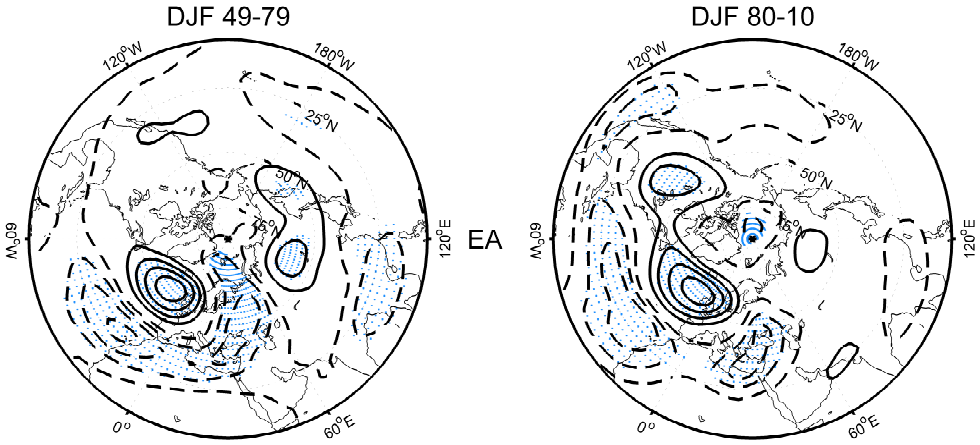

(b)

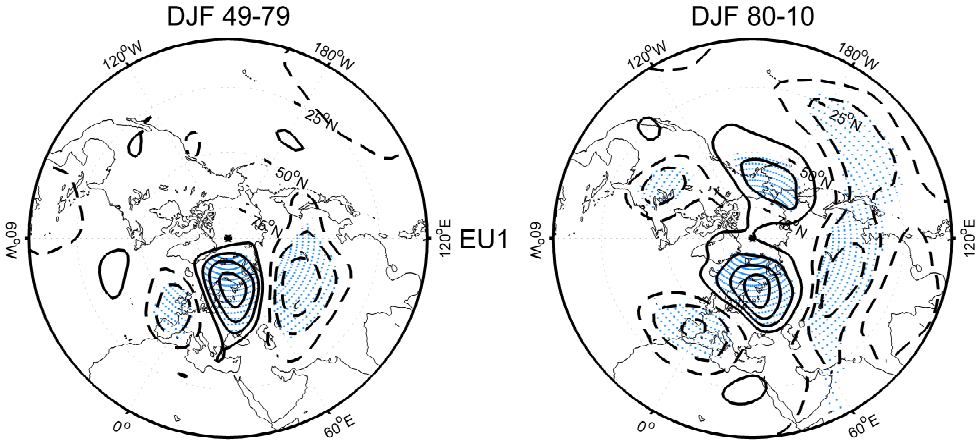

(c)

Figure 12: Z500 DJF patterns for a) PNA, b) EA, c) EU1 for both periods 1949-1979 (left) and 1980-2010 (right). The patterns are obtained by correlating the formal pattern index, as documented in this section and in Wallace and Gutzler (1981), with global northern hemisphere Z500. Negative correlations are dashed, contour interval is 0.2, the zero line is left out. Blue asterisks indicate statistical significance at the 95% confidence level.

80-100°E, and one also oppositely phased center over the Mediterranean and Spain around 35 - 50 °N, 10°E-20°W. It will be described using

$$EU1 = 0.5 \cdot Z(65°N, 37.5°E) - 0.25 \cdot Z(37.5°N, 90°E) - 0.25 \cdot Z(42.5°N, 5°W)$$

Figure 12 illustrates the spatial structure of the PNA, EA and EU1 pattern for the two independent periods 1949-1979 and 1979-2010. It is important to raise the question, to what extent the teleconnection patterns, which were described in this section, are stationary, reproducible features in the atmosphere. For example, it was shown that the centers of action of the NAO shifted towards the east in the period 1978-97 compared to the previous decades (Lu and Greatbatch, 2002, Jung et al., 2003). Wallace and Gutzler (1981) divided their available geopotential height data into two independent data sets in order to test for the reproducibility of their derived teleconnection patterns, but their data only covered 15 years. Here, we divide the available period of NCEP data into two subseries of equal length. The first covers the period 1949-1979, the second covers 1980-2010. Analogous to Wallace and Gutzler (1981), we computed the pattern indices for the PNA, EU1 and the EA pattern using the above mathematical expressions.

From Figure 12 it can be deduced that the correlations resemble those of Wallace and Gutzler (1981) very closely, and also the significant parts of the patterns seem to be stationary, since they coincide in most locations in the analysis of both periods. Differences in the patterns are also apparent. For example, in the later period, the EA pattern is correlated with a region over North America and the influence over Scandinavia becomes less important.

The three centers used to define the EU1 pattern seem to be in a stationary relationship, but in the later period, Z500 in the Pacific region and over North America is also significantly correlated with the index. Thus, between 30°and 45°N, there appears a circumglobal chain of centers of action, illustrated by the patches of negative correlation. This is an interesting feature, because it resembles the circumglobal summer teleconnection found by Ding and Wang (2005). This pattern will be discussed more in detail in section 6. However, one should keep in mind that a signal, which is dependent on a geographic location, does not necessarily mean that the atmospheric response to any kind of geographically fixed forcing is also a stationary feature. Greatbatch et al. (2004), for example, pointed out that the impact of ENSO on the whole European sector is not a robust feature on interdecadal timescales. In their regression analysis, the response over northern Europe even switches its sign between the periods 1958-77 and 1978-97. This should be kept in

mind when interpreting the results of the present study, since the regressions here only cover the satellite era.

2.6. Wave guides and Rossby wave source

Understanding the effect of Rossby wave propagation and dispersion on a rotating sphere is one key element in studies examining the atmospheric response to a certain prescribed forcing. Following the work of Sardeshmukh and Hoskins (1988), the central point is to find solutions to the vorticity equation:

$$\left(\frac{\partial}{\partial t} + \boldsymbol{v} \cdot \boldsymbol{\nabla}\right) q = S + F \tag{1}$$

where $q = \zeta + f$ is absolute vorticity, given by the sum of relative vorticity ζ and planetary vorticity f. S is a source term, which is referred to as the *Rossby wave source (RWS)*. The RWS is, from a classical perspective, associated with vortex stretching, and has been expressed in earlier studies simply as $-qD$, where D is divergence. After decomposing the flow field into its rotational and divergent components, Sardeshmukh and Hoskins (1988) pointed out the importance of including the effect of the advection of vorticity by the divergent flow field, which is usually associated with tropical upper tropospheric divergence. Putting this together, one gets the final expression for the RWS:

$$S = -\boldsymbol{v}_\chi \cdot \boldsymbol{\nabla} q - qD \tag{2}$$

where $\boldsymbol{v}_\chi$ is the divergent wind field. It has been shown that stationary Rossby waves cannot exist in a easterly flow regime (Webster and Holton, 1982). This stresses the importance of the geographical location of a RWS, that is associated with a specified forcing. Figure 13 shows DJF mean RWS for the period 1979 - 2011. The strongest RWS's are found in the vicinity of the North African/Asian jet, as well as in the Atlantic sector and in the central Pacific sector around 30°N, where the corresponding jet exit regions are located. The Indian part of the South Asian jet reveals strongest values. In the southern hemisphere,

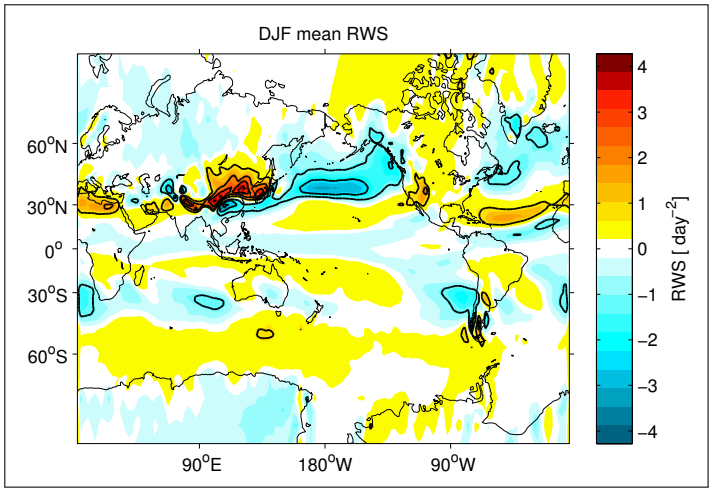

Figure 13: DJF mean RWS at 200 hPa from the NCEP/NCAR reanalysis. Contour interval is 1 day^{-2}.

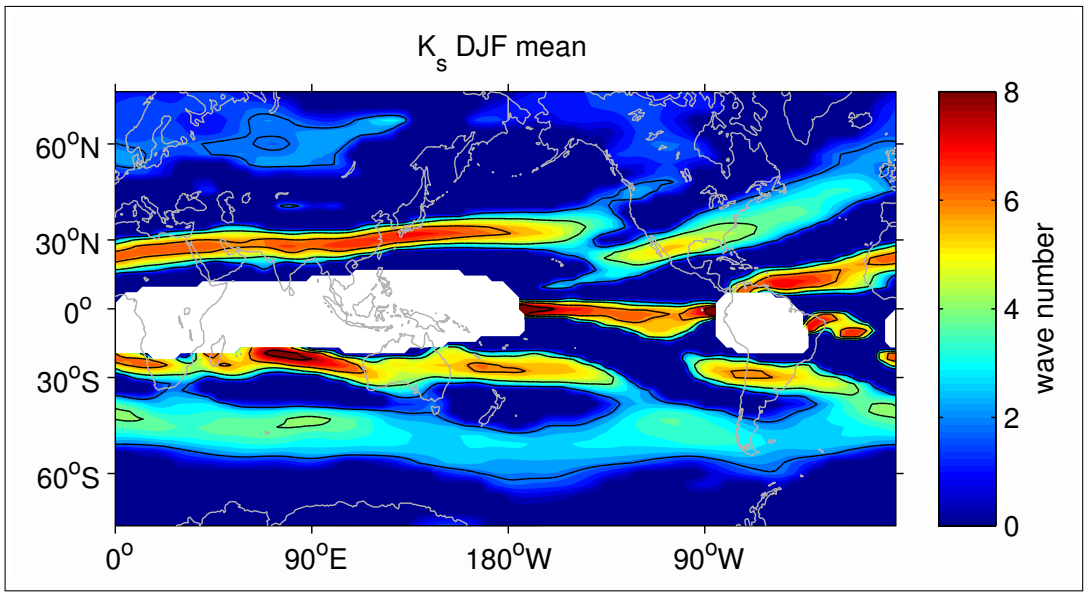

Figure 14: DJF mean K_S at 200 hPa in units of waves circling around a latitude band. Contour interval is 2. Regions that are not coloured are regions of mean easterlies.

there are regions of positive RWS south of the continents of Australia, South America and Africa. We note that these are regions of prevailing mean westerlies. In another study, Hoskins and Ambrizzi (1993) further analyse the characteristics of Rossby wave propagation. They find a critical zonal wave number for stationary Rossby waves in a westerly flow $\bar{U}$, which is

$$K_S = \left(\frac{\beta^*}{\bar{U}} \right)^{1/2} \tag{3}$$

where

$$\beta^* = \beta - \frac{\partial^2 \bar{U}}{\partial y^2} \tag{4}$$

is the meridional gradient of absolute vorticity. Hoskins and Ambrizzi (1993) further argue that Rossby waves will be refracted meridionally towards regions of larger K_S. Figure 14 reveals the existence of zonally aligned regions of maximum values of K_S, which are in good agreement with the location of the midlatitude jet streams. Their amplitude and location also agrees well with Figure 3 c) in Hoskins and Ambrizzi (1993). One may interpret these structures as Rossby wave guides and we note that an anomalous RWS, which is located within the vicinity of such a wave guide, can be effective in generating a global scale teleconnection due to Rossby wave propagation. As pointed out in Sardeshmukh and Hoskins (1988), diabatic heating in the equatorial region can induce anomalous RWS's in the subtropical westerlies, where it is effective in generating planetary wave motion. We will stress this theoretical concept in our analysis of local rainfall which initiates an anomalous RWS in regions where RWS driving is very effective.

3. Tropical Pacific teleconnections

3.1. ENSO teleconnections

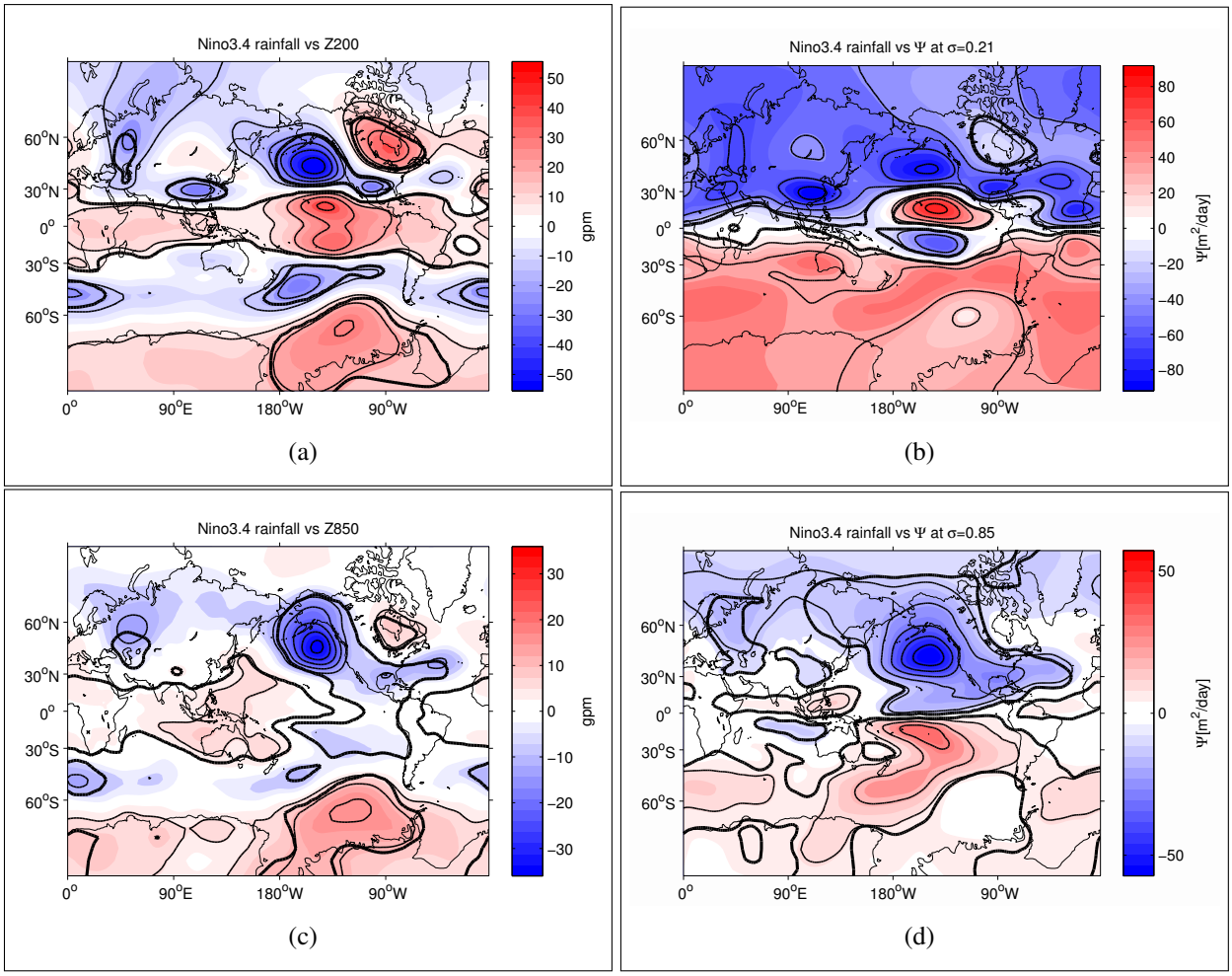

Figure 15: Maps using DJF mean data of (a) geopotential height at 200 hPa and (c) 850 hPa, and stream-function at σ levels (b) 0.21 and (d) 0.85 regressed onto Nino3.4 rainfall. The pattern corresponds to one standard deviation of the detrended rainfall time series. Contour interval is (a) 10 gpm, (b) 20 m^2/day, (c) 6 gpm, (d) 10 m^2/day. Negative (positive) values are highlighted blue (red), bold contours mark significance of the regression slope at the 95% confidence level. Corresponding rainfall time series is shown in Figure 9.

Anomalous heating in the eastern tropical Pacific has been shown in many studies to initiate global scale anomalies in the atmospheric circulation. For example, Trenberth et al. (1998) describe how anomalous heating associated with ENSO perturbs the atmosphere, and how the perturbation spreads towards the extratropics, including changes in the Hadley cell circulation in the meridional-vertical plane, as well as upper level divergence and lower level convergence of anomalous zonal winds in the heating region. We provide evidence for the existence of preferred teleconnection patterns for ENSO related diabatic heating using the 1980-2011 satellite ensemble mean rainfall as a

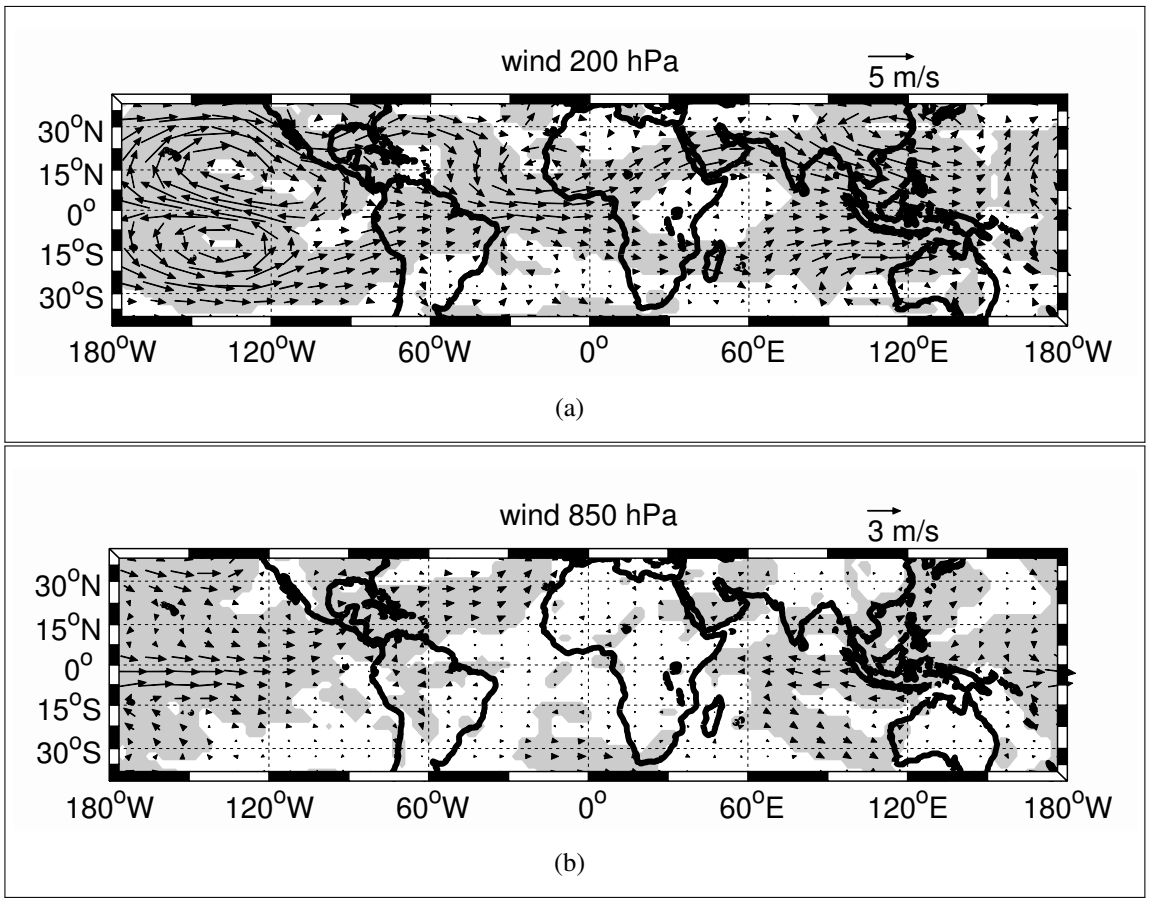

Figure 16: DJF Nino3.4 rainfall regressed on wind in (a) 200 hPa and (b) 850h Pa, grey shading marks significance of the regression slope at the 95% confidence level. The pattern corresponds to one standard deviation of the detrended Nino3.4 rainfall series.

representation of diabatic heating. Figure 15 shows atmospheric circulation patterns that are associated with Nino3.4 rainfall. At 200 hPa, a positive circumglobal Z200 anomaly can be identified along the equator, indicating anomalous high geopotential height in the troposphere, associated with the warming of the tropical band during an El Niño.

Another main result, which seems to be in general agreement amongst the tropospheric regression maps in this study, is that the atmospheric response has a strong barotropic component in the extratropics, while the responses seem to be rather baroclinic in the tropics. Z500 regressions were performed as well, but given their strong similarities to the Z200 regression maps, they are not shown. Nino3.4 rainfall is associated with significant strengthening of the Aleutian low, and anomalous positive Z200 over Hudson Bay. This is well known to be part of the PNA pattern (see section 2.6), although the positive anomaly over Hawaii is only apparent in Z200, while the negative anomaly center over the Gulf of Mexico is more clearly to see in the Z850 regression. The correlation coefficient of Nino3.4 rainfall and the PNA pattern index, as defined in section 2.6, is 0.63. There is also a teleconnection to the Southern hemisphere, which involves a structure somewhat similar to the Pacific South American (PSA) pattern (Mo and Peagle, 2001), that is,

anomalous high pressure between southern South America and the Ross Sea and anomalous low pressure at the same longitudinal position around 45°S. The amplitudes and spatial structure of both PNA and PSA patterns in the regressions show a remarkable degree of equatorial symmetry. Trenberth et al. (1998) argue, that the PNA pattern might be largely the response to ENSO related tropical heating in the Pacific, although a fraction of variability of the PNA pattern dynamics is due to internal atmospheric variability. They further assess the PSA pattern to be the Southern hemisphere counterpart of PNA pattern, or even the "footprint" of ENSO in the Southern hemisphere. We present regressions on streamfunction shown in Figure 15 b) and d), because close to the equator, the geostrophic approximation breaks down, and geopotential height may not be an appropriate indicator for the tropospheric flow. However, we wish to also highlight the tropospheric response close to the equator. At upper tropospheric levels (σ=0.21), there are two equator-symmetric anticyclonic anomalies found north and south of the equator west of the associated Nino3.4 rainfall box. This is consistent with theory (Gill, 1980). Spreading north-eastwards and south-eastwards off the equator, they closely follow the teleconnection structures in the geopotential height. The process for exciting such far-reaching teleconnections is explained in Trenberth et al. (1998): Above the forcing region, there is meridional outflow at upper tropospheric levels, which leads to upper tropospheric convergence in the subtropics, and thus, generation of anomalous high pressure and enhanced anticyclonicity there. Trenberth et al. (1998) further argue that this anomalous divergent wind can act as Rossby wave source in order to initiate the Rossby wave response that carries the information about the tropical disturbances towards higher latitudes, finally setting the well documented teleconnection patterns. However, the existence of those two upper-tropospheric anticyclones west to the region of equatorial heating is a very fundamental feature of the atmospheric response in all of our regressions that are associated with *tropical* rainfall, although weaker in most other cases. The tropical regression patterns presented in this section are in agreement with what is expected from linear theory (Gill, 1980), indicating that the nature of the response in the tropics is mainly governed by linear dynamics.

Regarding the patterns in Figure 15, we finally point out two more aspects. First, the pattern in Figure 15 a) and b) projects on a negative phase of the Southern Annular Mode (SAM), such that an impact on Antarctic climate and the Southern Ocean is possible (Ding et al., 2015). Second, the significant negative anomaly over Cape Hatteras in Figure 15 c) implies a remote impact on climate over this part of the Gulf Stream. In fact, DJF rainfall in our Gulf Stream box is correlated with the Nino3.4 rainfall at 0.39, which is significant at the 95% confidence level (see Table 2).

Figure 16 shows anomalous wind that corresponds to anomalous rainfall in the Nino3.4 box. At 200 hPa, the aforementioned anticyclones in each hemisphere are well established. Furthermore, the anomalous winds clearly depict the patterns which are associated with ENSO, namely low-level zonal divergence over the Maritime Continent, which includes anomalous westerly flow along the entire tropical Pacific, and anomalous easterly flow over the tropical Indian ocean. The structure of the regression pattern is reversed at 200 hPa, giving convergence over the western tropical Pacific, with easterlies (westerlies) over the eastern tropical Pacific (Maritime Continent). Regarding the response over the Pacific, the pattern mirrors an anomalously weak Walker - Cell Circulation, which is a circulation in the zonal-vertical plane and has first been described by Walker and Bliss (1932).

The baroclinic nature of the anomalous wind pattern may be viewed as the thermal wind response to a warming of the tropical troposphere. Via the thermal wind balance ($\frac{\partial T}{\partial y} \sim \frac{\partial u}{\partial z}$), the meridional gradient of the temperature in the troposphere is associated with vertical shear of the zonal winds.

We note that the amplitude of the patterns shown in Figure 16 correspond to anomalous Nino3.4 rainfall of one standard deviation, which equals 2.7 mm/day (see Fig. 9). We note that during years of strong El Niños, like those in the winters 1982/83, 1991/92, 1997/98, this rain rate was exceeded by a factor of up to 3. Thus, in those particular winters, the climatological mean easterlies can be reversed over parts of the tropical Pacific Ocean.

Finally, we highlight the importance of Rossby wave propagation for setting up the teleconnection and carrying the information about tropical upper tropospheric divergence towards higher latitudes. Figure 17 shows the anomalous Rossby wave source (RWS) at 200 hPa which is associated with enhanced rainfall in the Nino3.4 box. We note the significant anomalies in the North Pacific, centred at about 180°W, 36°N, and

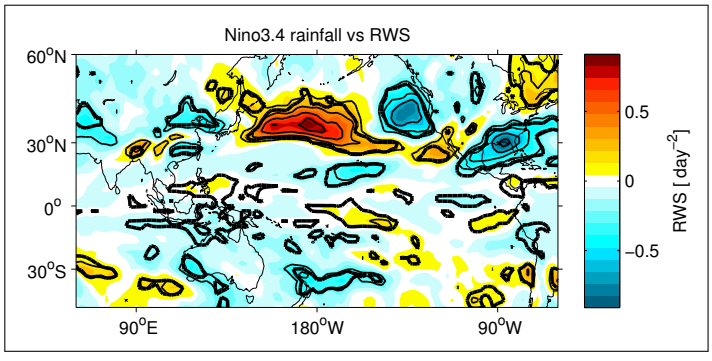

Figure 17: DJF RWS at 200 hPa regressed on Nino3.4 rainfall, contour interval is 0.2 day^{-2}. Negative (positive) values are highlighted blue (red). Bold contour indicates the 95% confidence level of the regression slope.

140°W, 40°N. These anomalies of enhanced (reduced) RWS reach values of up to 0.8 day^{-2}, and their geographical location coincides well with the DJF mean position of the Pacific jet (particularly its exit region, compare Fig. 29 in section 4). We thus suggest an important role for the North Pacific jet in generating and maintaining the northern hemisphere teleconnective response to ENSO-related tropical heating. Comparing with Figure 15 (a), it seems consistent that the anomalous positive (negative) RWS's in the North Pacific are crucial in generating the cyclone (anticyclone), that is associated with the PNA pattern.

ENSO stratospheric teleconnections

ENSO teleconnections at stratospheric levels are currently a subject of enhanced interest and discussion (see, for example Ineson and Scaife, 2009, Butler et al., 2014). It is assumed that, while the tropospheric teleconnections associated with ENSO affect the North Pacific and northern North America, the ENSO-related stratospheric impact mainly has consequences for northern Europe and Eurasia (Butler et al., 2014). The role of *Stratospheric Sudden Warmings* (SSWs) in manipulating the ENSO teleconnection will be briefly discussed in this section.

Figure 18 shows Z50 regressed on Nino3.4 rainfall and a composite map of anomalous Z50 for winters when both El Niño and SSWs occurred. We therefore use the same ENSO and SSW events as Butler et al. (2014), which were defined as follows. ENSO winters are winters, when the SST anomaly in the Nino3.4 box [5°N - 5°S, 170°W - 120°W] exceeds 0.5°C for five consecutive three-month seasons, whose months overlap (NDJ, DJF, JFM, etc.). For a SSW to occur, daily 10 hPa zonal winds at 60°N must turn from climatological westerlies to easterlies in at least one of the winter months from November to March. In Figure 18 (a), however, significance is only exhibited for the center over Hudson Bay and Scandinavia. We also note the significant positive anomalies south of 30°N in the entire Northern Hemisphere, consistent with the tropical-wide impact of El Niños on the atmosphere. We decided to show a composite map for only those El Niño winters, which also exhibited a SSW (Figure 18 (b)). This is found in only five of the investigated winters, which is not sufficient to motivate a regression analysis (see figure caption in Fig. 18 for details). One can see that the stratospheric response looks somewhat different, when only considering SSW years, although this result is only significant at the 90% confidence level. The center of anomalous positive Z50 shifted from Hudson Bay to Greenland, while the negative pressure anomaly rather appears as a zonally aligned band in subpolar latitudes. In their model composite, Ineson and Scaife (2009) find this stratospheric signal propagating downward and show that it leads to

cold temperatures in Northern Europe and warm temperatures in Southern Europe by setting the transition to a negative phase of the Arctic Oscillation.

The findings of Ineson and Scaife (2009) indicate that even the European *surface* response to ENSO is complicated by having a different structure in winters when SSW occur, compared to winters without SSWs. Ineson and Scaife (2009) find that in ENSO years without SSWs, Europe is governed by a negative NAO-like structure at sea level pressure, with cold air over Northern Europe and Scandinavia. Ineson and Scaife (2009) argue that in ENSO years with SSWs, however, the SLP response resembles the negative phase of the NAM, with enhanced pressure over the polar cap and Greenland, and reduced pressure in a zonal band at subpolar latitudes. Another complication for analysing the connection to ENSO is given by the fact that both El Niño *and* La Niña conditions seem to enhance the probability for a SSW in late winter (Butler et al., 2014).

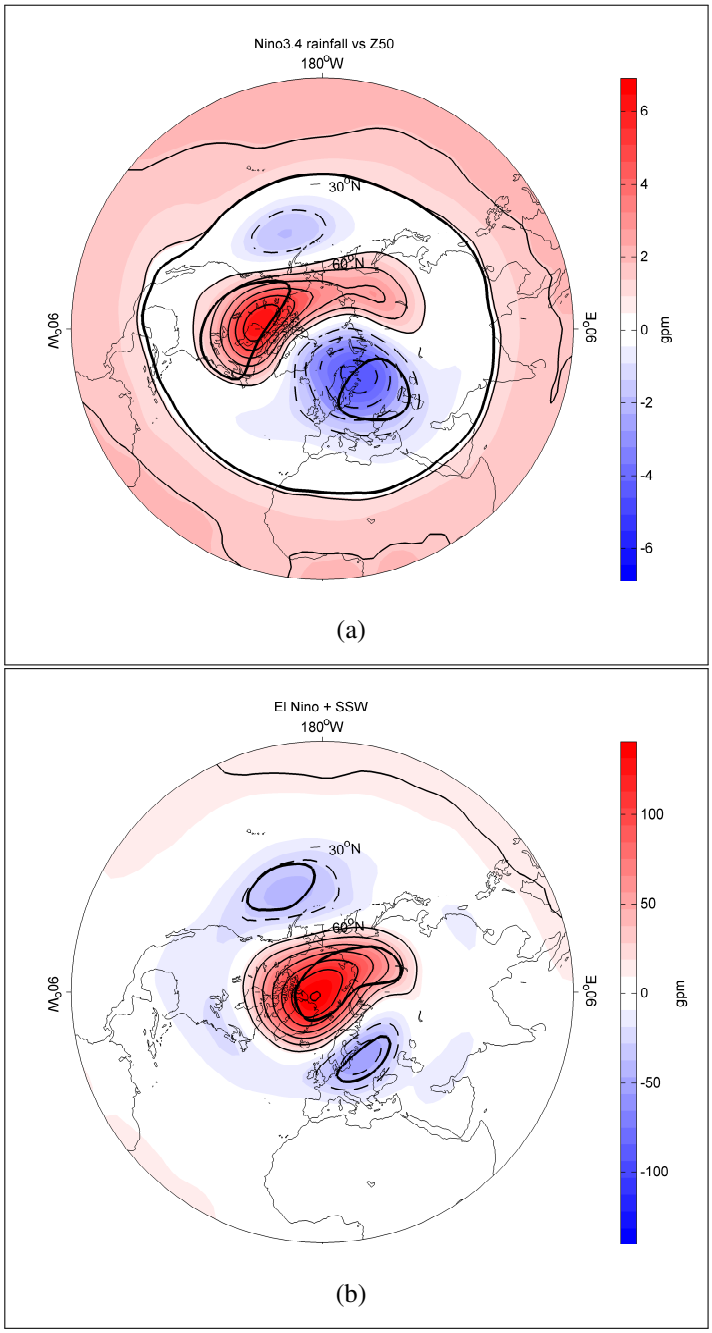

Figure 18: Lower stratosphere: (a) Z50 regressed on Nino3.4 rainfall, contour interval is 1 gpm. Negative values are dashed. Bold contour indicates the 95% confidence level of the regression slope. (b) composite map of anomalous Z50 in El Niño years which also exhibited a SSW [following Butler et al. (2014), but for satellite-era only. Corresponding winters are 86/87,87/88,02/03,06/07,09/10]. Contour interval is 20 gpm. Bold contour encloses regions where the composite is different from non-composite years at the 90% confidence level. (in no place, significance is found to exceed 95%).

Figure 19 is used to demonstrate the role of ENSO in manipulating the SSW surface signature in Northern Europe. In both a) and b) (SSW during ENSO neutral *and* El Niño), one can see

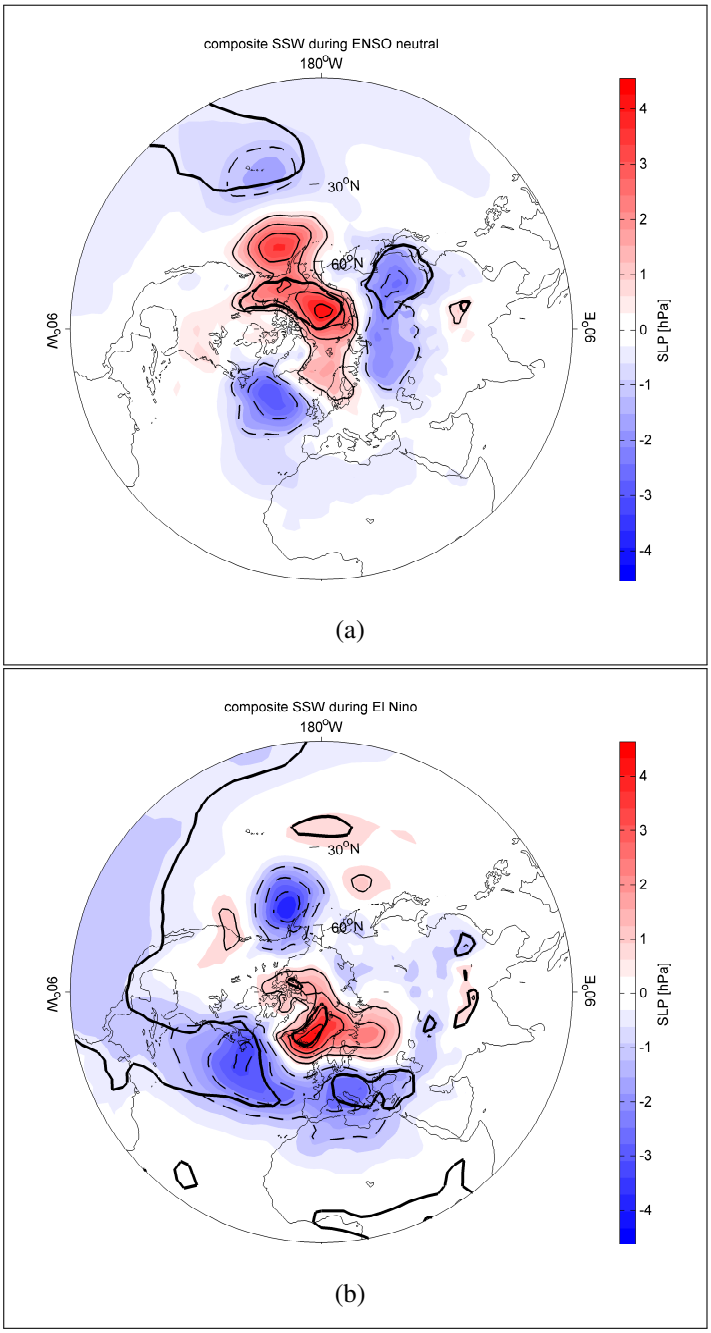

Figure 19: Composite maps of anomalous SLP in (a) SSW winters during ENSO neutral and (b) SSW winters during ENSO+ . In a), the corresponding winters are 79/80,81/82,01/02,03/04. In b), the same winters are considered as in figure 18 b). Contour interval is 1 hPa, negative values are dashed. Bold contour encloses regions where the composite is different from non-composite years at the 95% confidence level.

anomalous high SLP over the pole and anomalous low SLP in subpolar regions in the zonal band around 60°N. One exception is the amplitude of the Aleutian low, which is anomalously strong during SSWs that coincide with El Niño, and anomalously weak during SSWs at ENSO neutral phases. However, three interesting differences can be seen in the pattern in Figure 19 a) and b). First, in the El Niño case, the polar center of anomalous high pressure is shifted southward to Iceland and there is a ridge identified over northeast Russia. Second, the significant negative SLP anomaly over northern Asia and Russia in Figure 19 (a) is not evident any more in the case of SSW during El Niño. Third, the subpolar trough rather extends through the entire Atlantic-European sector in the case of El Niño -coinciding SSWs, while in the case of ENSO-neutral SSWs, there is no signal over central Europe. Thus, the pattern in Figure 19 b) projects more strongly on the negative phase of the NAO, which goes along with reduced advection of moist marine air over Europe. This could explain the cold, dry conditions in Northern Europe and Eurasia, and the warm, moist conditions in Southern Europe/ Eurasia mentioned in Ineson and Scaife (2009), which occur during El Niño events, when the stratosphere is "active".

As a concluding note in this section, we emphasize that the results regarding the composites of ENSO-related rainfall during SSWs lack statistical significance when compared to the regressions. This is because the observational period only covers five years when both El Ninño and SSWs occurred. We therefore conclude that the above results concerning SSWs are suggestive rather than conclusive.

In this section, the well documented ENSO teleconnections could be reproduced using the satellite ensemble mean rainfall as a proxy for diabatic heating in the tropical Pacific, which underlines the quality and potential of the satellite rainfall estimates in the period after 1979. We note that this was not the case when we used the NCEP/NCAR rainfall for the period from 1949 to present. This motivates us to investigate the teleconnections that are associated with diabatic heating in other regions.

3.2. Central Pacific teleconnections

There are studies supporting a recent shift of the El Niño activity, and its associated SST anomalies in the tropical Pacific to the west (Ashok et al., 2007, Weng et al., 2009, for example). These studies find that in recent decades the characteristic warming of the SST during El Niño events occurs in the central Pacific, rather than in the eastern part of the basin, which was the case in earlier decades. This new type of El Niño with negative tropical Pacific SST anomalies in the east and west, and positive anomalies in the central Pacific is referred to as *El Niño Modoki*. In fact, Ashok and Yamagata (2009) point out that El Niño Modoki is a mode of variability that is distinct from El Niño. It is thus suggested that ENSO changes its behaviour in the context of a warming world, such that El Niño Modoki may occur more often in future, compared to the classical El Niño (Ashok and Yamagata, 2009). Therefore, we include a Central Pacific (CP) rainfall box in our analysis, in order to examine teleconnections emerging from anomalous diabatic heating in the central Pacific. Figure 20 shows anomalous atmospheric circulation that is related to rainfall in the CP rainfall box, which is

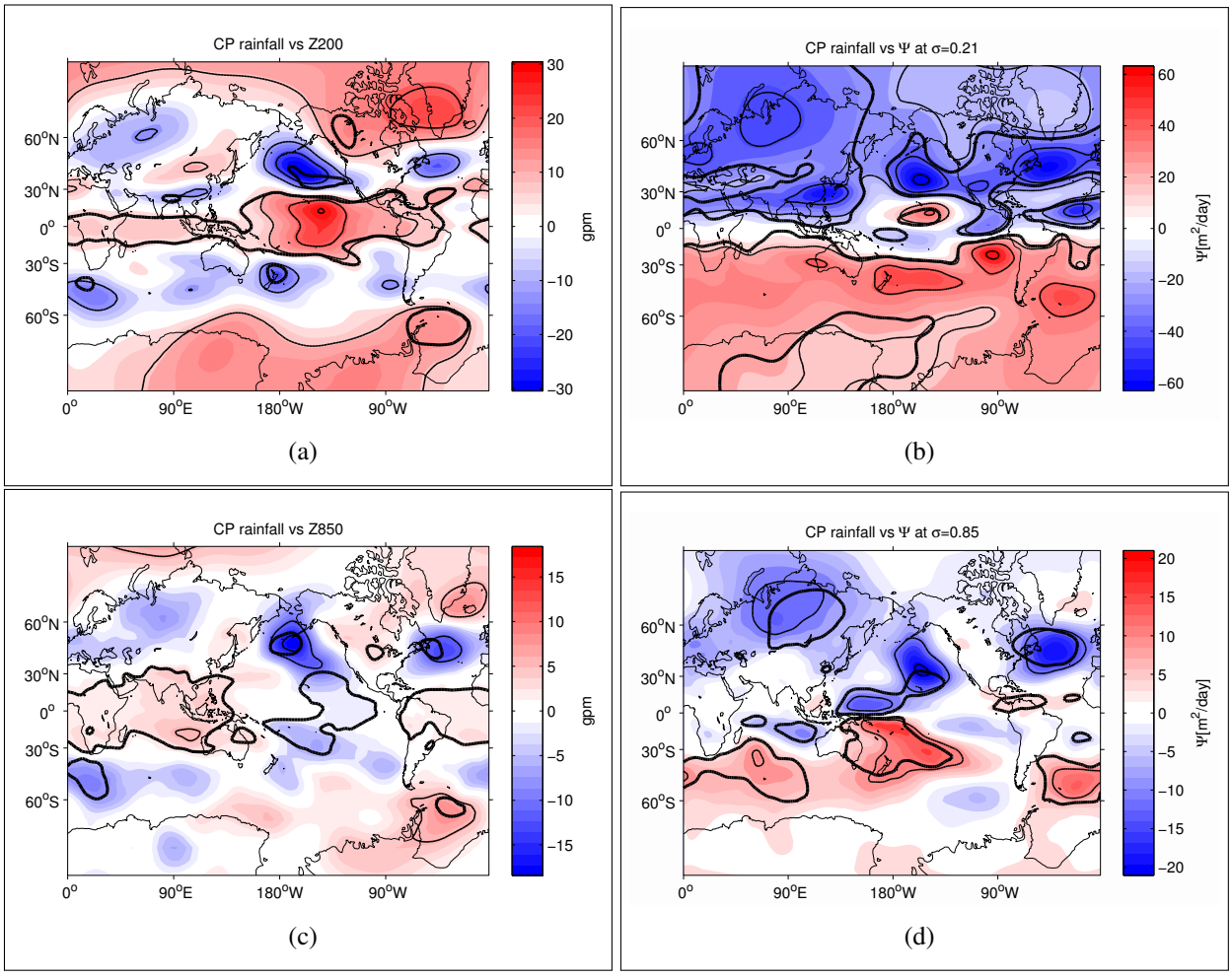

Figure 20: as Figure 15, but regressions are done on CP rainfall. CP rainfall time series is shown in Figure 9.

located west to the Nino3.4 box (see Figure 9 for the CP rainfall time series). Note that the effect of Nino3.4 rainfall has been removed from the CP rainfall. Analysing the patterns, and comparing them to the respective patterns associated with Nino3.4 rainfall (Figure 15), we are pointing out two important features. First, the overall structure of the patterns, for both streamfunction and geopotential height, bear a high degree of similarity, although our CP rainfall is by definition not correlated to Nino3.4 rainfall. The patterns in Figure 20 seem to be shifted somewhat westward when compared to Figure 15, which is consistent with the westward shifted rainfall box, when compared to Figure 15. It also compares well with Sardeshmukh and Hoskins (1988), who stress the insensitivity of the extratropical response to the exact location of a forcing in the tropical Pacific. Second, the overall amplitude of the regression patterns is weaker, as expected for all rainfall time series which do not contain any Nino3.4 rainfall signal anymore, since a remarkable fraction of variability is removed when using this technique.

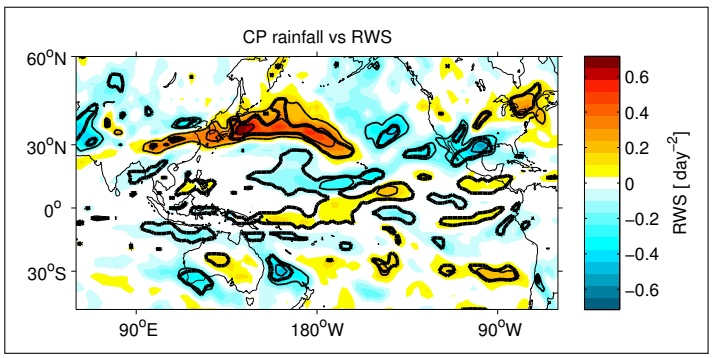

Figure 21: DJF RWS at 200 hPa regressed onto CP rainfall, contour interval is 0.2 day^{-2}. Negative (positive) values are highlighted blue (red). Bold contour indicates the 95% confidence level of the regression slope.

There are, however, also differences in the patterns, when compared to Figure 15. For example, the two equator-symmetric anticyclones at upper tropospheric levels west of the rainfall region (Fig. 20 b) are weaker and bear a less pronounced structure. Also, the patterns in Figure 20 a) and c) do not project significantly on the PNA pattern (r = 0.22), because the whole extratropical response is shifted westward, and exhibits only local significance across the North American continent. Especially the Aleutian low is located more to the Central Northern Pacific, and is detached from the North American coast. A projection on the Pacific South American pattern, as can be seen in the case of Nino3.4 rainfall, cannot be detected in Figure 20 a) and c). In all four panels in Figure 20, one can see a hint of a projection onto the negative phase of the NAO, although not significant at the 95% confidence level (r = -0.25). This can be seen in the anomalous low geopotential height over the midlatitude North Atlantic (negative streamfunction) and anomalous positive geopotential height over Greenland/Iceland (positive streamfunction).

We note that the regression pattern looks somewhat different when ENSO is not being removed (not shown). In that case, there is a stronger projection on the PNA- and PSA pattern, since CP

rainfall is significantly positive correlated with Nino3.4 rainfall (see Table 2).

However, although for CP rainfall there is no significant correlation found with the classical teleconnection patterns, the atmosphere is significantly affected in the tropics, as well as in higher latitudes. The shape of the regression pattern is similar, but not identical to the one found for teleconnections induced by rainfall in the Nino3.4 box in the last section.

In Figure 21, the CP rainfall - related anomalous RWS is shown. It is striking that, even in the absence of any Nino3.4 rainfall signal, significant positive RWS structures are revealed in the western North Pacific, at about 30°- 45°N, 100°E - 150°W. It is still located in the vicinity of the Asian/Pacific jet, but shifted somewhat westward, when compared to Figure 17, consistent with the more westward located features in Figure 20.

3.3. Maritime Continent teleconnections

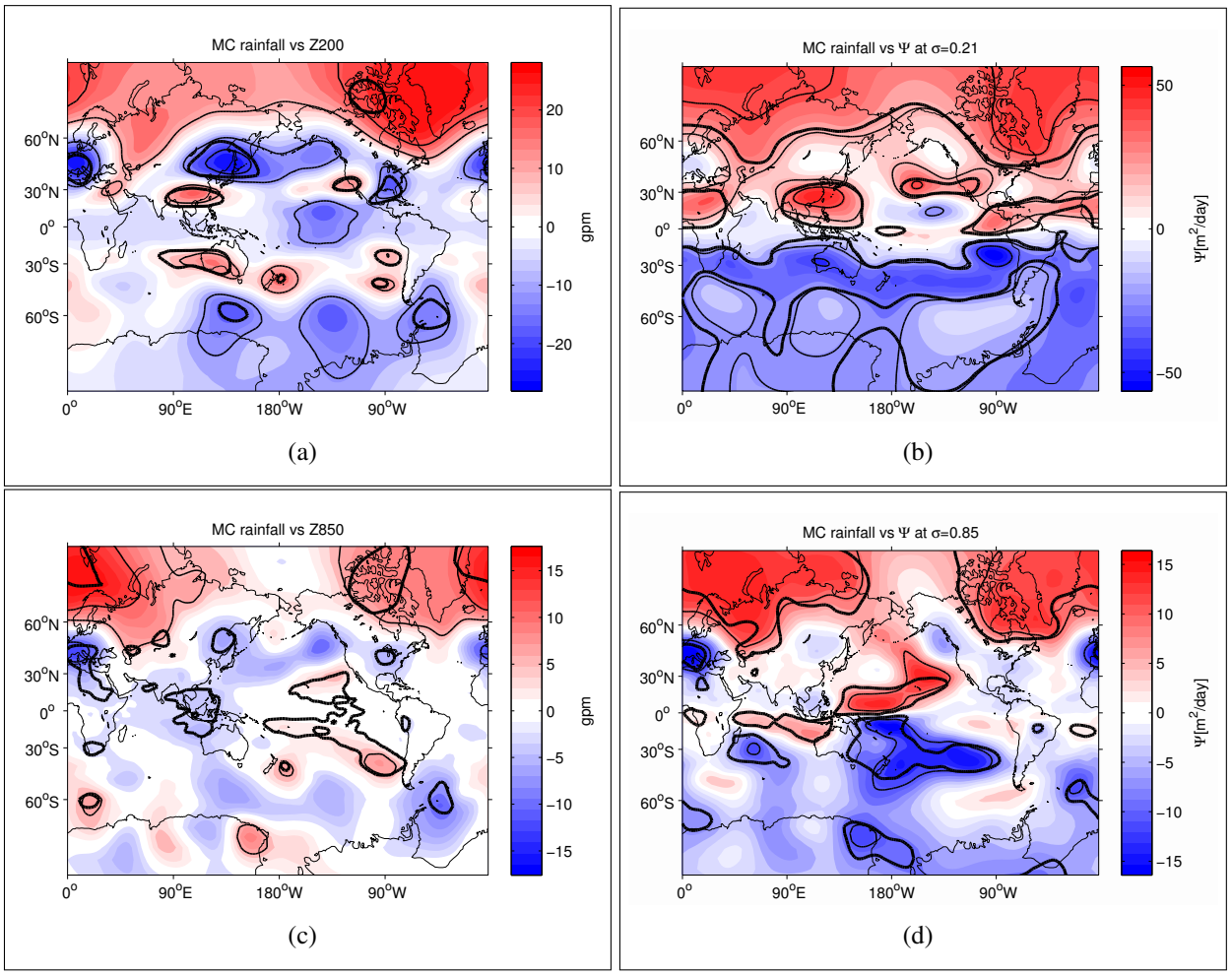

Figure 22: as Figure 15, but regressions are done on MC rainfall. MC rainfall time series is shown in Figure 9.

In Figure 3, it was shown that the Maritime Continent (MC) has a strong rainfall variability in boreal winter. On the other hand, Figure 9 indicates that a large fraction of this variability is due to the MC rainfall connection to ENSO. In fact, MC rainfall and Nino3.4 rainfall are correlated at -0.85 (see Table 2). Hence, if removing ENSO from the MC rainfall, the resulting rainfall time series is dominated by low frequency vari-

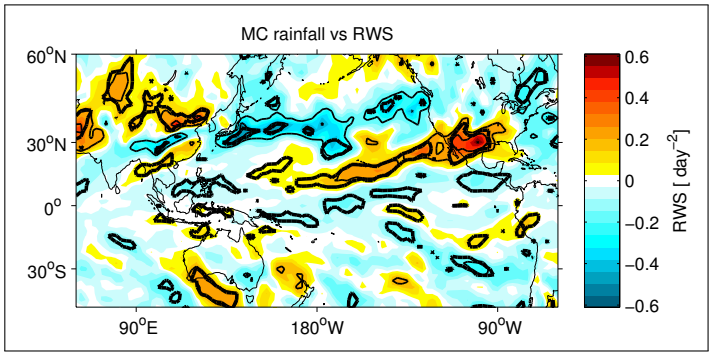

Figure 23: DJF RWS at 200 hPa regressed onto MC rainfall, contour interval is 0.2 day^{-2}. Negative (positive) values are highlighted blue (red). Bold contour indicates the 95% confidence level of the regression slope.

ability, and the overall variability is reduced by 47% (see Figure 9). Figure 22 indicates that anomalous Maritime Continent (MC) rainfall is connected to atmospheric circulation structures at various locations throughout the globe. Analogous to the results from the two previous sections, panel a) reveals an equator-symmetric response, which spreads north-eastward and south-eastward from the region of the Maritime Continent as wave trains. This includes two pronounced anticyclones over south east China and western Australia, which are accompanied by significant relative cyclonic structures over north-east China and between Tasmania and Antarctica, respectively. These results are in good agreement with Sardeshmukh and Hoskins (1988, their figs. 4 e), g)), who find the same poleward spread of perturbation streamfunction response, in the case of a heating placed over Indonesia.

Regarding the anomalous RWS pattern for the case of MC rainfall (Fig. 23), significant positive anomalies appear north of the MC, between Beijing and Korea, and directly south of Australia. Thus, the RWS anomalies are embedded in the Asian/Pacific jet and the southern hemisphere subtropical jet, respectively. Bearing in mind the potential of the jet streams to act as Rossby wave guides, this strengthens our hypothesis that MC convection can drive extratropical Rossby wave responses of global scale.

The upper-tropospheric circulation seems to be affected over North- and South America as well, which suggests the existence a wavetrain over the high latitude Pacific ocean connecting these regions with the Maritime Continent. When looking at Figure 22 b), the structure is governed by mainly negative (positive) anomalies in the Southern (Northern) hemisphere. To some degree, this prohibits our analysis to detect a wavetrain of centers with alternating signs, but centers of *relative* anomalies (with respect to the background) can be seen over the Pacific around the latitudes of 50-60°N/S, respectively. Furthermore, the hint of a propagating wave-like pattern can be observed in figure 22 a), westward of 110°E at about 45°N, reaching well into the Atlantic sector. In a Z500 regression map (not shown), the positive anomaly over the Caspian sea is significant at the 95% confidence level.

Regarding the northern hemisphere subpolar region at about 60°N, it seems that the response occurs as a zonally varying wavelike pattern. Qualitatively, this is the case for any of our here presented wintertime Z200 regression maps. It is further consistent with the results of Branstator (2002), who analyses the solutions of the barotropic vorticity equation linearized about a mean DJF winter state. He finds 300mb responses to be meridionally confined to the subpolar jet, which

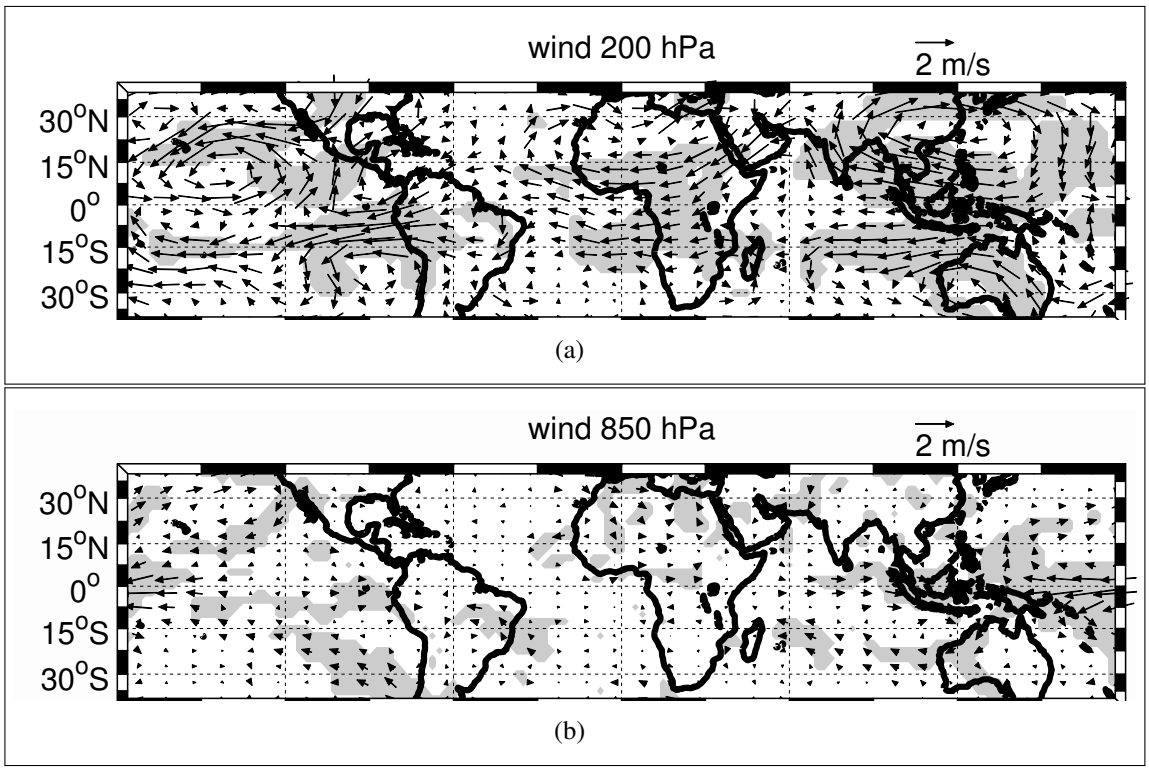

Figure 24: DJF MC rainfall regressed on wind in 200 hPa (a) and 850h Pa (b), grey shading marks significance of the regression slope at the 95% confidence level. The pattern corresponds to one standard deviation of the detrended MC rainfall time series.

acts as a waveguide and to be shaped as a zonally aligned chain of disturbances.

We emphasize that the teleconnections associated with MC rainfall are not simply given by the ENSO-related teleconnections with the sign reversed. One may expect this, because the MC rainfall is negatively correlated with the Nino3.4 rainfall (see Table 2). For example, when the ENSO signal is retained in the MC rainfall time series, the MC rainfall projects onto the negative phase of the PNA pattern (r = -0.44, significant at the 95% confidence level, not shown). However, when removing ENSO from the MC rainfall time series, the projection onto the PNA pattern is not evident anymore (r = 0.17, as suggested in Figure 22 (a)).

One feature in Z850 regression maps, which all the pattern presented here have in common, is the negative geopotential height anomaly over the corresponding rainfall box (see Fig. 22 c) for the case of MC rainfall), which is accompanied by zonal convergence of the zonal wind at that pressure level. It is consistent with a negative SLP anomaly in the rainfall region (not shown). As illustrated by Copsey et al. (2006), in the tropics, rising air due to enhanced diabatic heating causes pressure to rise at upper levels relative to neighbouring regions. The pressure gradients generate divergent flow out of the column of rising air, which results in reduced SLP.

Figure 24 shows anomalous wind at 200 and 850 hPa pressure levels which goes along with enhanced MC rainfall. At 850 hPa, one can see the strong zonal inflow of up to 2 m/s towards the MC. At the same time, there occurs significant poleward flow at 850 hPa over the MC, which is consistent with the idea of rising air stretching vortex lines in this "lower" level, which increases the absolute vorticity of the rising air parcels. As described in Gill (1980), parcels must achieve this change in vorticity by moving to latitudes with the same background vorticity (i.e. poleward). In his model study, he found poleward motion in the forcing region at lower levels, and equatorward motion at upper levels, which resulted from an equatorial heating. On the other hand, in the 200 hPa wind field, both strong anticyclones are observed over the MC, with amplitudes of up to 2 m/s, as well as significant westward flow in large parts of the tropics and subtropics. The anomalous 200 hPa wind over India also seems to impact the Indian winter monsoon circulation, with anomalous flow from the Indian ocean towards continental India.

4. Indian Ocean boreal winter teleconnections

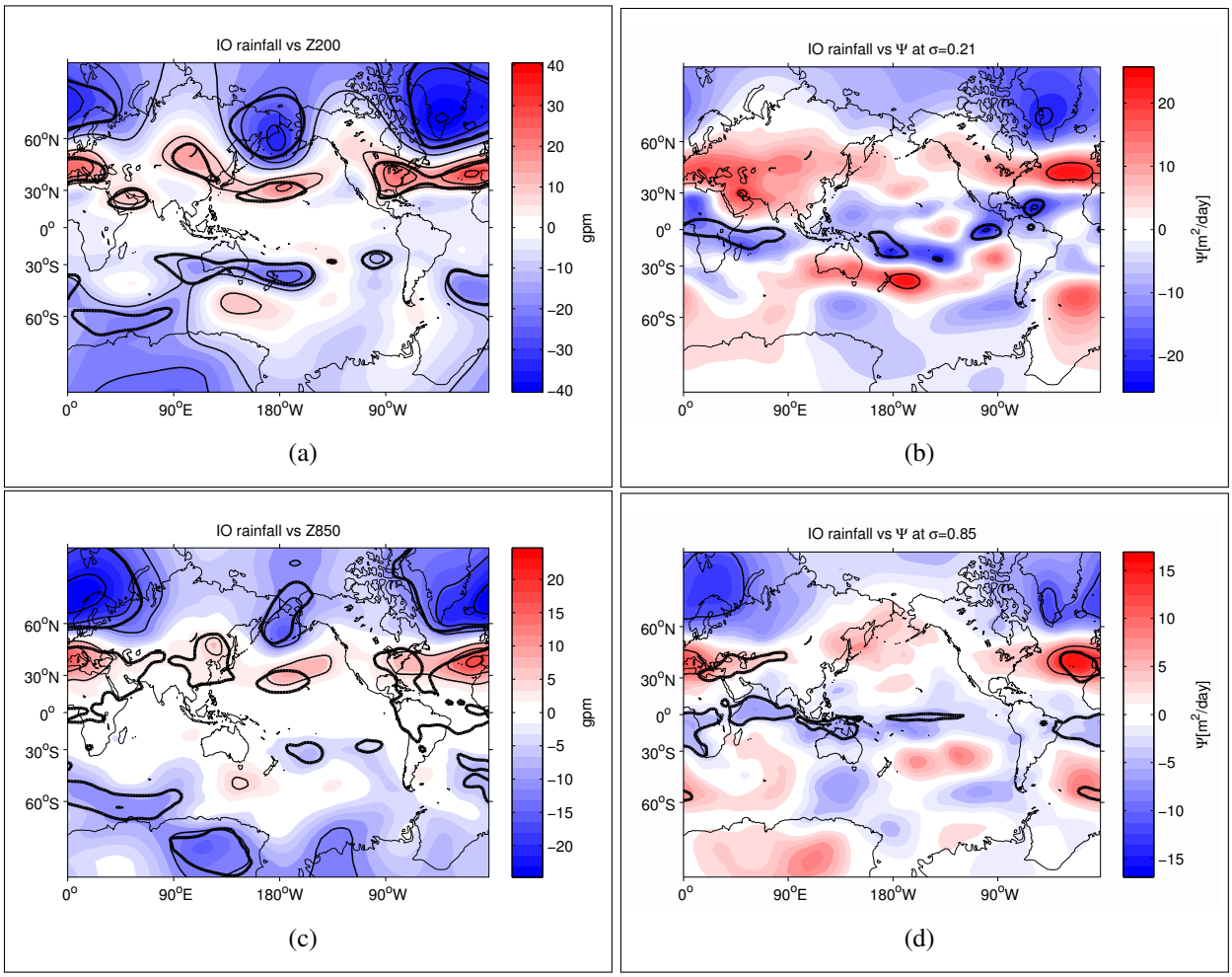

Figure 25: as Figure 15, but regressions are done on IO rainfall. IO rainfall time series is shown in Figure 9.

Figure 25 shows teleconnections associated with enhanced IO rainfall in DJF. The most outstanding feature to be seen is a significant projection onto the NAO/AO, which involves negative anomalies poleward of 60°N and circumglobal positive anomalies between 30 and 60°N. This feature is apparent at both 200 and 850 hPa height. We find correlation coefficients of 0.55 (0.51) between IO rainfall and the NAO (AO), both significant at the 95% confidence level. While not significant in streamfunction, in the Z200 regression there are also significant anomalies over the South Pacific region and over Australia, suggesting a poleward and eastward pathway in both hemispheres for atmospheric disturbances originating in the Tropical Indian Ocean (TIO). Moreover, in both Z850 and Z200 regressions, we find a significant positive anomaly over the central North Pacific, centred at about 180°W, 35°N, and a strong negative anomaly to the north.

In order to argument precisely, we will decide between the two terms *TIO*, that describes the

region of the tropical Indian Ocean in general, and *IO*, which refers to the distinct region of our IO rainfall box, as described in Table 1. However, the outstanding projection on the NAO/AO, which are the dominant patterns of northern hemisphere atmospheric variability (Hurrell et al., 2003) is further examined. We computed the corresponding AO (NAO) pattern and time series via an EOF analysis of the northern hemisphere (Atlantic sector) Z850. In Figure 26 (a) and (b), the correlation between the AO/NAO PC series and the rainfall over the Indian Ocean in DJF is shown. The link between equatorial IO rainfall and AO/NAO is clearly identified by the significant positive correlation coefficients of 0.4 to 0.5, which span the central TIO for both AO and NAO PC series.

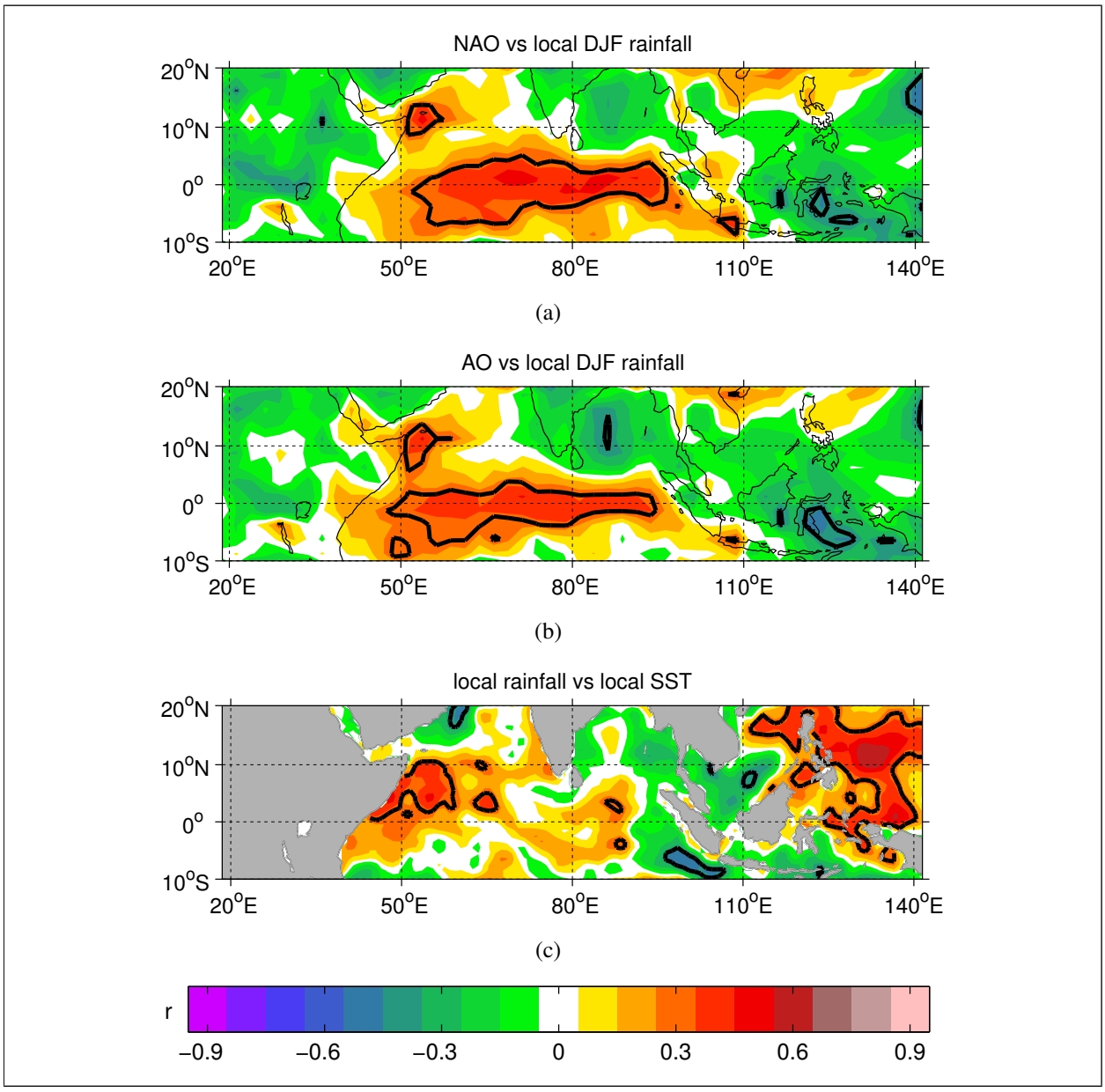

Figure 26: Detrended local DJF mean rainfall in the Indian Ocean region correlated with (a) NAO index, (b) AO index, (c) local SST. Shown is the correlation coefficient. Colour contouring in steps of 0.1. Black line indicates the 95% confidence level of the correlation. NAO and AO indices are shown in Figure 11.

There are numerous studies that have suggested this winter-time link between heating anomalies over the Indian Ocean and Northern hemisphere circulation. A thorough analysis of this linkage is beyond the scope of this study, but we will present the most prominent hypotheses about underlying physical processes, and test, whether we can confirm them in our regression analysis of various atmospheric parameters. In the following, several aspects of the TIO rainfall - northern hemisphere circulation links are highlighted and examined.

The DJF TIO rainfall is independent of underlying TIO SST

In general, enhanced tropical ocean SSTs favour enhanced precipitation at the same site (Trenberth et al., 1998, Copsey et al., 2006, for example). The latter authors claim there is a lack of historical observational rainfall data in the Indian Ocean to consolidate this relation in that region. In our DJF analysis, however, we can confirm the parallel behaviour of SST and rainfall for the tropical Pacific ocean, but not for the TIO. Figure 26 (c) shows the correlation coefficient of local DJF rainfall and local SST at every grid point in the tropical Indian-Pacific Ocean region. Except for some spots in the western TIO, equatorial SSTs are not significantly correlated with local rainfall in the TIO in DJF. Another analysis (not shown) reveals that the IO box rainfall is not significantly correlated to local SSTs anywhere in the tropical TIO. This is an interesting result because there are studies connecting the positive TIO SST trend in recent decades with the trend of the winter NAO towards more positive index values in the second half of the twentieth century (Hoerling et al., 2001, 2004, Bader and Latif, 2005, Copsey et al., 2006). However, it is interesting that both enhanced SST and rainfall in TIO are discussed to project onto positive polarity of the NAO/NAM (Hoerling et al., 2001, Bader and Latif, 2005), while at the same time we find SST and rainfall are not significantly correlated with each other on a DJF mean basis. However, one must be aware of the rainfall - SST relationships in the model studies of Hoerling et al. (2001) and Bader and Latif (2005). In these studies, anomalous rainfall is associated with warm SST anomalies, which is not what we observe in winter.

To further underline this, Figure 27 shows the correlation of local TIO rainfall and the NAO PC series, but this time the linear effect of local underlying SST has been removed from the local rainfall at every grid point. One can see that the significant positive correlations of TIO rainfall with the time series of the NAO are still identified, and are, perhaps, even stronger than before. This clarifies that the TIO rainfall, which projects onto the positive polarity of the NAO/AO in

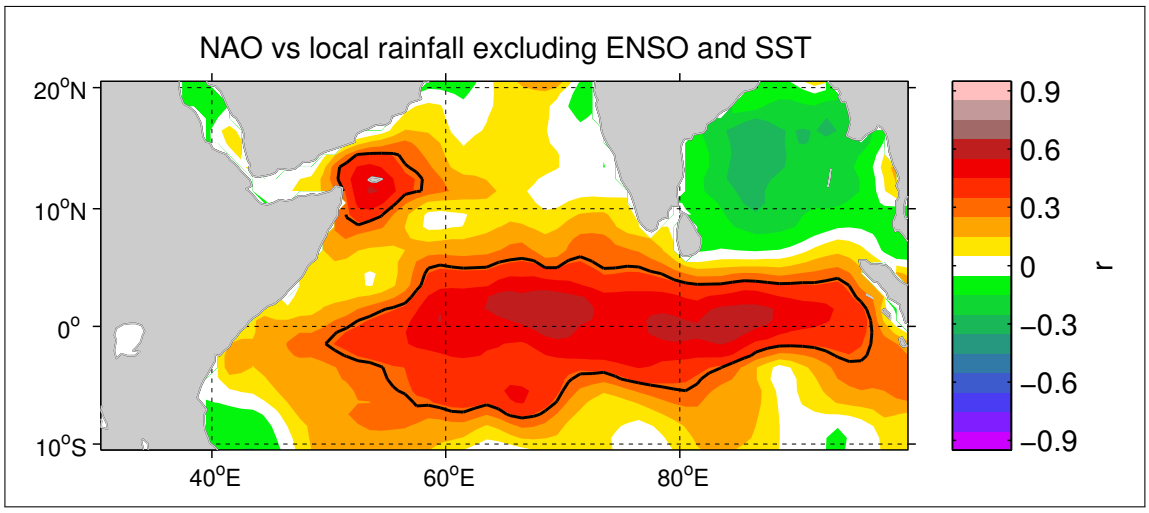

Figure 27: Correlation coefficient of NAO time series and local rainfall in DJF, but the effect of underlying SST at each grid point has been removed from the rainfall. All time series are detrended, colour contouring in steps of 0.1. The black line indicates the 95% confidence level of the correlation

DJF, is independent of the underlying TIO SST. This result is in contradiction with the hypothesis of Bader and Latif (2005), who link the positive IO SST trend in the last century to the positive NAO trend, assuming that the increased SST is the main driver for insitu TIO precipitation to finally drive the atmosphere via enhanced latent heat release.

To shed light on this issue, one needs to examine what processes, rather than SST, control DJF rainfall in TIO. The Madden Julian Oscillation [MJO, Madden and Julian (1972)] is an atmospheric phenomenon that affects TIO and the Western Tropical Pacific (WTP) regions on intra-seasonal (30-90 days) time scales. The MJO is a complex three-dimensional system that propagates eastward at about 5 m/s, while if affects various atmospheric variables. See Zhang (2005) for a thorough review of the MJO. For this study, the most important aspect of the MJO is that it organizes precipitation along the equatorial Indian - and Western Pacific ocean, with a localized region of enhanced deep convective activity and, thus, enhanced rainfall, which propagates eastward during one MJO cycle. Thus, we suggest DJF rainfall in our Indian Ocean box is in large part controlled by the MJO, and its interannual variability.

It is noteworthy, that the link between TIO and the NAO/AO is significantly apparent in our analysis for *both* IO rainfall including and excluding the Nino3.4 signal. This is not straightforward to expect, because ENSO can explain a significant part of TIO rainfall variability (see Table 2). This finding is in concert with Gong et al. (2014), who removed both the impact of ENSO and Indian Ocean Dipole (IOD) events from their data and still found a projection on the NAM. In the

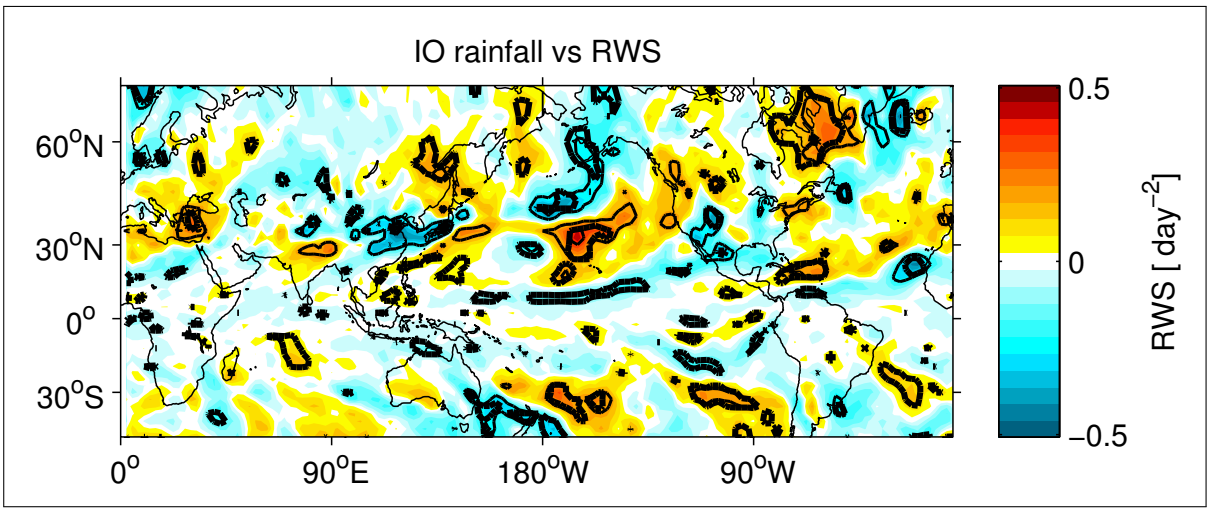

Figure 28: DJF RWS at 200 hPa regressed onto IO rainfall, contour interval is 0.2 day^{-2}. Negative (positive) values are highlighted blue (red). Bold contour indicates the 95% confidence level of the regression slope.

following, we will briefly present a condensed summary of how the interaction between NAO/AO an TIO rainfall is believed to work, and which physical processes are involved. We will discuss whether we can find evidence for the hypotheses in our analysis.

How TIO rainfall may control NAO/AO

There are several studies proposing theories of how TIO convection, that may be associated with MJO-related rainfall, can project onto the northern hemisphere atmospheric circulation, especially onto the NAO/AO (Zhou and Miller, 2005, Cassou, 2008, L'Heureux and Higgins, 2008, for example). In a recent study, Lin et al. (2015) point out that variability in winter mean convective activity associated with the MJO over the tropical Indian Ocean generates disturbances in the South Asian jet. Lin et al. (2015) claim that these disturbances are connected to the circumglobal pattern discussed in Branstator (2002), which communicates the teleconnection response to MJO convective activity through the northern hemisphere. Furthermore, Lin et al. (2015) find that enhanced rainfall over the Indian Ocean is associated with the positive phase of the NAO, as found here.

We now analyse anomalous RWS that corresponds to TIO rainfall. Figure 28 reveals a positive RWS anomaly over India, embedded in the climatological jet at about 30°N, but it is not significant at the 95% confidence level. In Figure 28, we therefore note the significant negative RWS anomalies over China and Japan, and the positive RWS anomaly north of it, at about 55°N. These features may be responsible for the generation of the Z200 anomalies over the central northern Pacific in Figure 25 (a). In the Pacific jet exit region between 30°and 50°N, anomalous RWS's

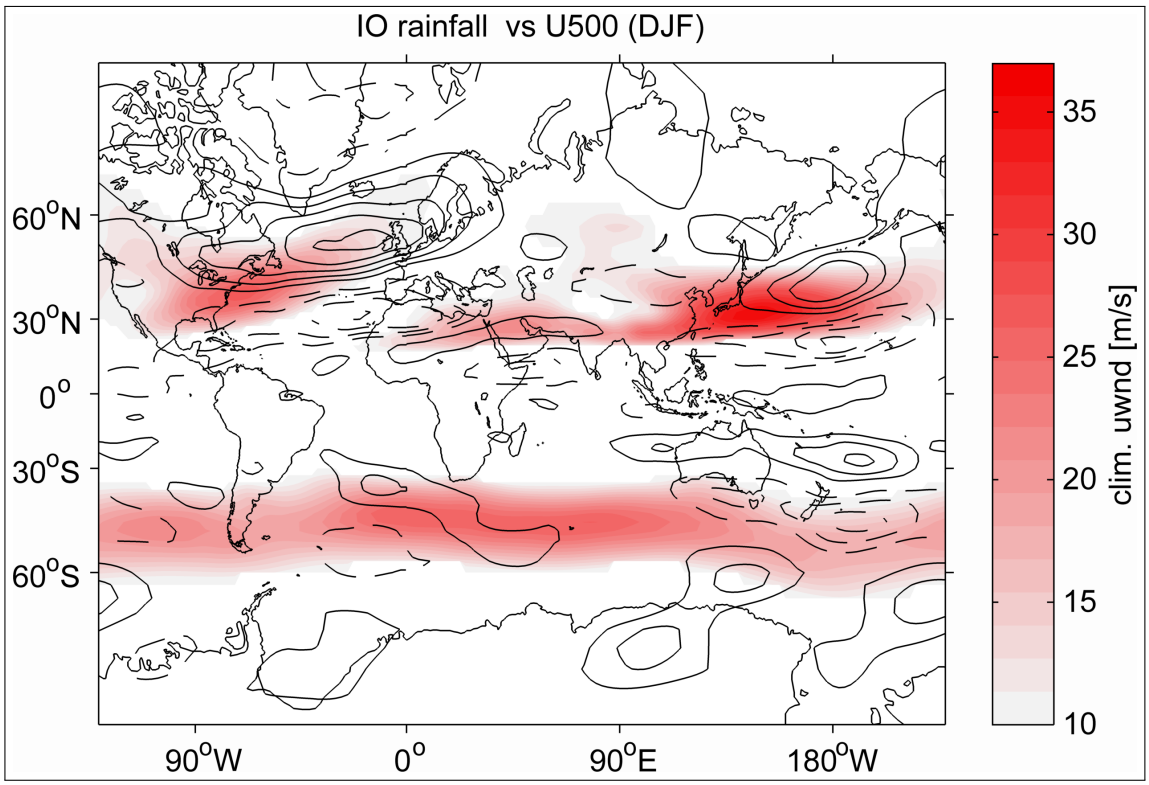

Figure 29: DJF IO box rainfall regressed onto 500 hPa zonal wind (contours). Negative (westward) zonal winds are dashed, contour interval is 0.4 m/s, the zero line is not plotted. Colour shading shows the climatological DJF mean zonal wind, with only westerly winds exceeding 10 m/s shown.

are found as well. This is consistent with Zhou and Miller (2005), who claim it is more likely for the MJO to force the NAO than vice versa. They explain how MJO induced planetary waves can influence the extratropical circulation via the meridional propagation of Rossby waves in the Pacific sector.

Figure 28 also reveals significant positive RWS features between Hudson Bay and Greenland. Clearly, this feature is responsible for the generation of the cyclonic (negative) anomalies over Greenland in Figure 25. This result is supported by Lin et al. (2009), who suggest that MJO convective activity provides an additional forcing mechanism for the NAO. They find that MJO convection is linked to the NAO via a Rossby wave train in the Pacific sector. Cassou (2008) finds that when MJO convective activity is located over the TIO, a Rossby wave train is generated over the Western Pacific. He notes that 10 days later, the probability for positive NAO phase is significantly enhanced, hence corroborating the role of the MJO as a precursor for the NAO. Indeed, Figure 29 reveals a pattern of alternating signs of anomalous zonal wind spanning the western Pacific area in both hemispheres. L'Heureux and Higgins (2008) point out the importance of the jet exit region in the North Pacific area. They find a linear positive NAO response after phases 2-4 of the

MJO. Following the index nomenclature of Wheeler and Hendon (2004), phase 2-4 corresponds to enhanced rainfall in the vicinity of the TIO. Comparing with Figure 29, the climatological jet exit region is rather sharply defined at about 170°E, 35°N. This is even more clearly to see in 200 hPa (not shown). However, the overlaid TIO rainfall response suggests a slight northward shift of the jet exit, with anomalous eastward (westward) winds north (south) of the climatological jet. This structure is consistent with the anomalous high Z200 feature over the North Pacific [Figure 25 a)]. The dynamics of the MJO teleconnection towards the northern Pacific may be the key to understanding the projection onto the positive phase NAM, especially in the context of nonlinearity of the response with respect to the position of the jet stream exit.

Amongst all of our examined DJF rainfall boxes, except Nino3.4, IO rainfall is the only one which is associated with a significant large scale stratospheric teleconnection. Figure 30 shows IO rainfall regressed on Z50. One can clearly identify the positive phase of the NAM, underlining that this teleconnection is valid even at stratospheric levels. It has been show that one center of the MJO - related tropospheric teleconnection in the North Pacific sector is collocated with a climatological trough (Garfinkel et al., 2012, and references therein). According to that, Garfinkel et al. (2012) suggest that the teleconnection pattern can constructively interfere with the climatological standing wave, which leads to enhanced polar vortex wave driving and explains the tendency of SSWs to follow certain phases of the MJO, while a Pacific pathway is suggested to connect these regions. The observed MJO-AO/NAO lag correlation (MJO leading) is shown to be of the order of $\approx$ 2 weeks for the tropospheric part of the teleconnection (L'Heureux and Higgins, 2008, Lin et al., 2009). Garfinkel et al. (2012), for the stratospheric link, find lags of $\approx$ 40 days. However, the fact that certain NAO/AO

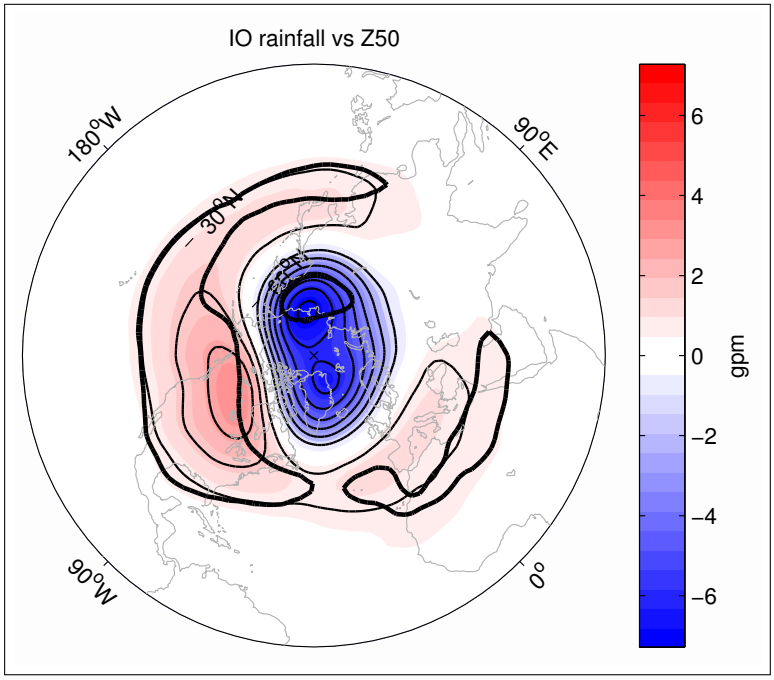

Figure 30: DJF IO box rainfall regressed onto Z50. Contour interval is 1 gpm. Negative (positive) values are highlighted blue (red). Bold contour marks significance of the regression slope at the 95% confidence level.

phases tend to follow certain MJO phases points towards the role of MJO driving the NAO/AO, rather than vice versa.

How the NAO/AO may control TIO rainfall

There seems to be a consensus amongst most studies that MJO related TIO rainfall triggers/manipulates the NAO/AO (Zhou and Miller, 2005, Cassou, 2008, Lin et al., 2009), rather than vice versa. Nevertheless, a two-way connection of these regions might be of dynamical importance for the observed link (Lin et al., 2009). There are, however, also studies explaining possible mechanisms of how the NAO/AO may lead to enhanced rainfall in TIO. Zhou and Miller (2005) point out that during a *negative* AO phase, planetary waves tend to propagate upwards and polewards to the polar stratosphere, which then leads to anomalous sinking (rising) motion in polar (tropical) regions. They claim, that these motions in the tropics are associated with tropical diabatic *cooling*, which affects circulation and temperature profiles, and thus, may manipulate the MJO.
On the other hand, Lin et al. (2009) show that the NAO forces an anomalous zonal wind pattern in the Atlantic/Africa region at 200 hPa height, propagating south-eastward towards the Indian ocean. They suggest this may lead to an MJO development. This process is examined more in detail in Gong et al. (2014), although they find maximum JFM NAO/AO - TIO rainfall correlations in the Southern Indian Ocean (5-10°S, 60 -80 °E), while we find maximum correlations around the equator (see Fig. 26 (a), (b)). Following the hypothesis of Gong et al. (2014), during positive NAO/AO winters, a strong tropospheric Rossby wave train is apparent in the Atlantic sector in JFM, causing anomalous high geopotential height over the Arabian peninsula at 20°- 30°N, 55°-70°E. This corresponds to a strengthening of the Arabian high, and it is accompanied by anomalous anticyclonicity and downward motion there. They further argue that the enhanced near surface pressure of the strengthened Arabian high, together with the anomalous southward wind over the near surface northern Indian Ocean leads to a stronger Intertropical Convergence Zone (ITCZ), and thus, enhanced TIO rainfall. We test this hypothesis with our regression analysis for consistency. Indeed, in Figure 25 one can see a projection onto the positive Arabian high in 200 hPa, and Figure 29 reveals that in mid-troposphere this goes along with anomalous eastward flow at the vicinity of the North African/Asian jet between 20°- 30°N, and anomalous westward flow to its south, between 0°- 15°N. This is consistent with anticylonic flow and the westerly flow may be interpreted as a strengthened North African/Asian jet, since the pattern is collocated with the climatological maximum of zonal winds. At 925 hPa, we also find weak but significant southward flow over the Northern Indian Ocean south of the Indian peninsula (not shown), which is in agreement with the

hypothesis of a strengthened ITCZ. We do, however, not find any significant signal in the meridional wind at 200, 500, or 925 hPa, that would be consistent with the anticyclonic anomaly over the Arabian peninsula and would contribute to a strengthening of the Arabian high. The structure of the anomalous pattern of 500 hPa zonal wind in Figure 29, which extends from the North Atlantic south-eastward towards the TIO, might be indicative of a Rossby wave train, as in Lin (2009).

5. Gulf Stream boreal winter teleconnections

It was pointed out by Held et al. (2002) that the strongest global diabatic heating rates may be divided into two groups around the globe. The first class corresponds to strong tropical diabatic heating, following the large scale equatorial convective systems, which is likely to be connected to positive SST anomalies. We have considered this class in the previous sections. The second class is the strong diabatic heating in midlatitudes, where convective activity tends to follow the warm SSTs along the path of the Gulf Stream (GU) and Kuroshio current. In Figure 3 it can clearly be seen that enhanced rainfall variability follows the associated warm SSTs in parts of the Atlantic and Pacific Ocean at latitudes around 30°- 40°N. Keeping this in mind, Held et al. (2002) pointed out that the tropospheric response to this extratropical heating is mainly given by motion in the "great circles". Figure 31 shows anomalous geopotential at 200 and 850 hPa, as well as anomalous meridional wind at 200 hPa, which are related to enhanced GU rainfall (again, with the ENSO signal removed). In contrast to Held et al. (2002), we do not find well defined streamfunction responses that are organized in great circles (not shown). Rather, the associated Z200 - and Z850 patterns bear some resemblance to the circumpolar wave train mentioned in Branstator (2002), although significance of the centers of action is exhibited only at a few grid points. However, in Figure 31 a), wave number 2 activity is detected in polar latitudes north of 58°N. There is a suggestion of a wave train, starting in the Gulf Stream region of the Atlantic Ocean, bending north-eastward over Europe and then south-eastward over Eurasia, to finally die out in the western Pacific Ocean. To further shed light on this teleconnection, we regressed meridional wind onto GU rainfall and overlaid the climatological zonal wind to highlight the jet core (see figure 31 b)). Again, one can see wave number 2 activity in polar regions in the Northern hemisphere, and the centres of action of the Europe/Eurasia wave train between 30°and 60°N appear as significant structures. We note that these disturbances appear at the northern flank of the Africa/Asian Jet stream core, which is consistent with the findings of Branstator (2002), who finds strongest streamfunction variability in the wintertime northern hemisphere to be organized as wavelike structures around the jet stream core. Interestingly, there is also the suggestion of a wavelike structure in the southern hemisphere.

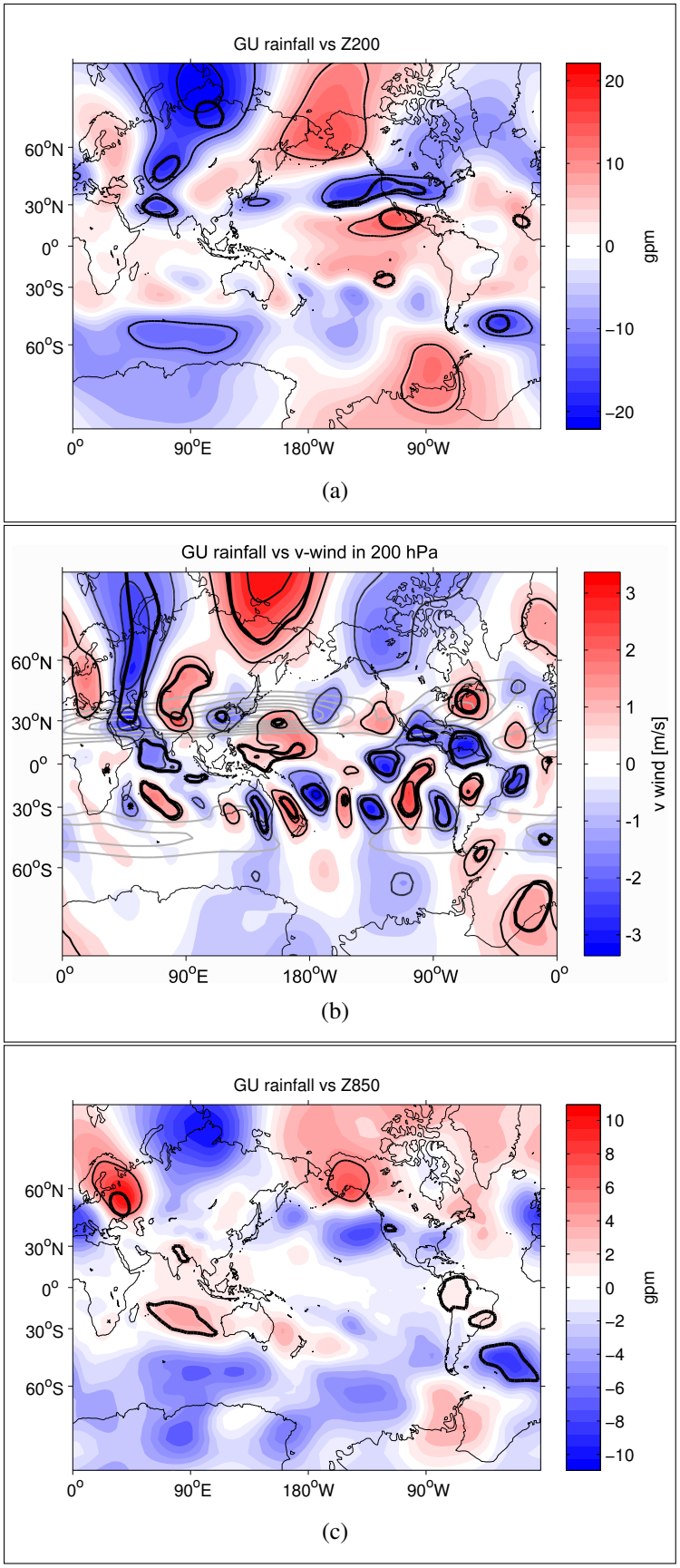

Figure 31: a): DJF regression of GU rainfall on Z200, contour interval is 10 gpm, negative values are dashed. The bold solid line marks the 95% confidence level of the regression slope. **b)**: GU rainfall regressed on meridional wind. Contour interval is 0.4 m/s. Gray contours additional mark the climatological zonal wind. Contour interval is 8 m/s. **c)** as a), but GU rainfall is regressed onto Z850. Contour interval is 6 gpm.

It is located at the northern edge of the southern hemisphere circumglobal jet, and the anticyclones/cyclones are as large as 20° of latitude and longitude, respectively. The idea that enhanced convection over the warm water region of the Gulf Stream can impact the troposphere has a long history (Ratcliffe and Murray, 1970, Rodwell and Folland, 2002). However, it is not entirely clear if enhanced convection over the Gulf Stream can lead to tropospheric responses of global scale. As an example, Minobe et al. (2008) show that enhanced rainfall over the Gulf stream goes along with low level convergence and upper level divergence in the region of the Gulf Stream, which is generally consistent with large scale tropical convection. They hypothesize that the Gulf Stream can even have an impact on remote places in the troposphere via planetary wave driving, but these remote teleconnections are hard to distinguish from internal variability of the troposphere. Looking at Figure 31 b), one can indeed find significant divergence of the anomalous meridional winds in 200 hPa over Cape Hatteras. Is is noteworthy, that this divergence, and the associated atmospheric diabatic heating, are located in the vicinity of the Atlantic jet stream [see Figure 31 b)]. The fact that the diabatic heating in the case of GU rainfall is embedded in local westerlies may be of fundamental importance for the atmospheric response. Stationary Rossby waves cannot be supported in an easterly background flow regime, only in a mean westerly flow (Webster and Holton, 1982, for example). Therefore, the midlatitude wave train can be interpreted as Rossby wave disturbances, which are supported by the Atlantic/Eurasian jet.

Figure 32 provides a map of anomalous RWS at 200 hPa height, that is related to GU rainfall. We note the region of significant negative RWS anomalies over the GU box, indicating divergence. Apart from that, there are barely any larger scale features, but only several regions of anomalous

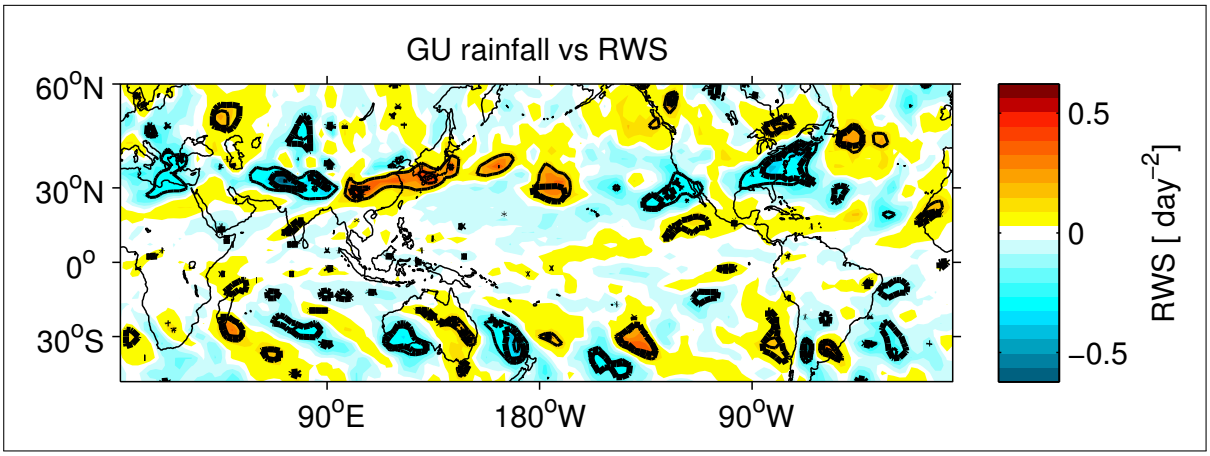

Figure 32: DJF RWS at 200 hPa regressed onto GU rainfall, contour interval is 0.2 day^{-2}. Negative (positive) values are highlighted blue (red). Bold contour indicates the 95% confidence level of the regression slope.

RWS in the vicinity of the subtropical jet in both hemispheres around 30°N and 30°S. This is in concert with our interpretation of the GU teleconnections being confined to the jets, but it does not entirely prove that enhanced GU diabatic heating excites those teleconnections. As noted by Branstator (2002), disturbances along the subtropical jet stream core are a dominant mode of internal variability in the tropospheric circulation. Since the Gulf Stream is located at the same meridional location as the jet, its rainfall variability may as well be impacted by the atmosphere's internal variability. However, the significant negative RWS feature over Cape Hatteras may be important for generating the wave train from the North Atlantic over Europe and Asia.

For the sake of completeness, we note that the zonal mean background flow in winter may be substantially different from the one in summer. This can be seen when comparing the latitudinal position of the midlatitude jet stream in Figure 29 and 33. In summer, the jet steam core is located more northward than in winter. This is why an atmospheric response to the same forcing may be different among other seasons because of their individual basic states. We conclude that this is one reason why we do not see similar tropospheric circulation patterns for our rainfall boxes in JJAS (not shown).

6. Indian Summer Monsoon teleconnections

Hitherto, we only examined teleconnections that occur in boreal winter, which is straightforward, since northern hemisphere atmospheric low frequency variability is most pronounced then (Blackmon, 1976). In fact, we carried out the same regression analysis for our rainfall boxes for the summer season (JJA, JAS and JJAS) as well, but for most of the equatorial-symmetric rainfall boxes, no trustworthy, largescale teleconnection pattern could be revealed. As can be seen in Figure 3 and 5, rainfall (variability) peaks in boreal summer in the India (IND), China (CH), and Sahel rainfall boxes. The Indian summer monsoon (ISM) is a process which controls the organization of atmospheric flow and associated rainfall over the Indian Subcontinent in summer to large parts. Figure 33 shows JJAS regressions of Z200 and Z850 on JJAS rainfall for both All India and satellite ensemble rainfall estimates. We test whether the ISM teleconnections are consistent among the satellite ensemble mean product and the All India rainfall product, which covers a different period (1949 - 2000) than the satellite era. Note that to allow for the comparison with the All India rainfall product, we computed the satellite ensemble for JJAS, as well. Consequently, we removed the Nino3.4 rainfall signal as a proxy for ENSO. This is done although IND rainfall and Nino3.4 rainfall are not significantly correlated with each other in JJAS (r = -0.16) and although Lin (2009)

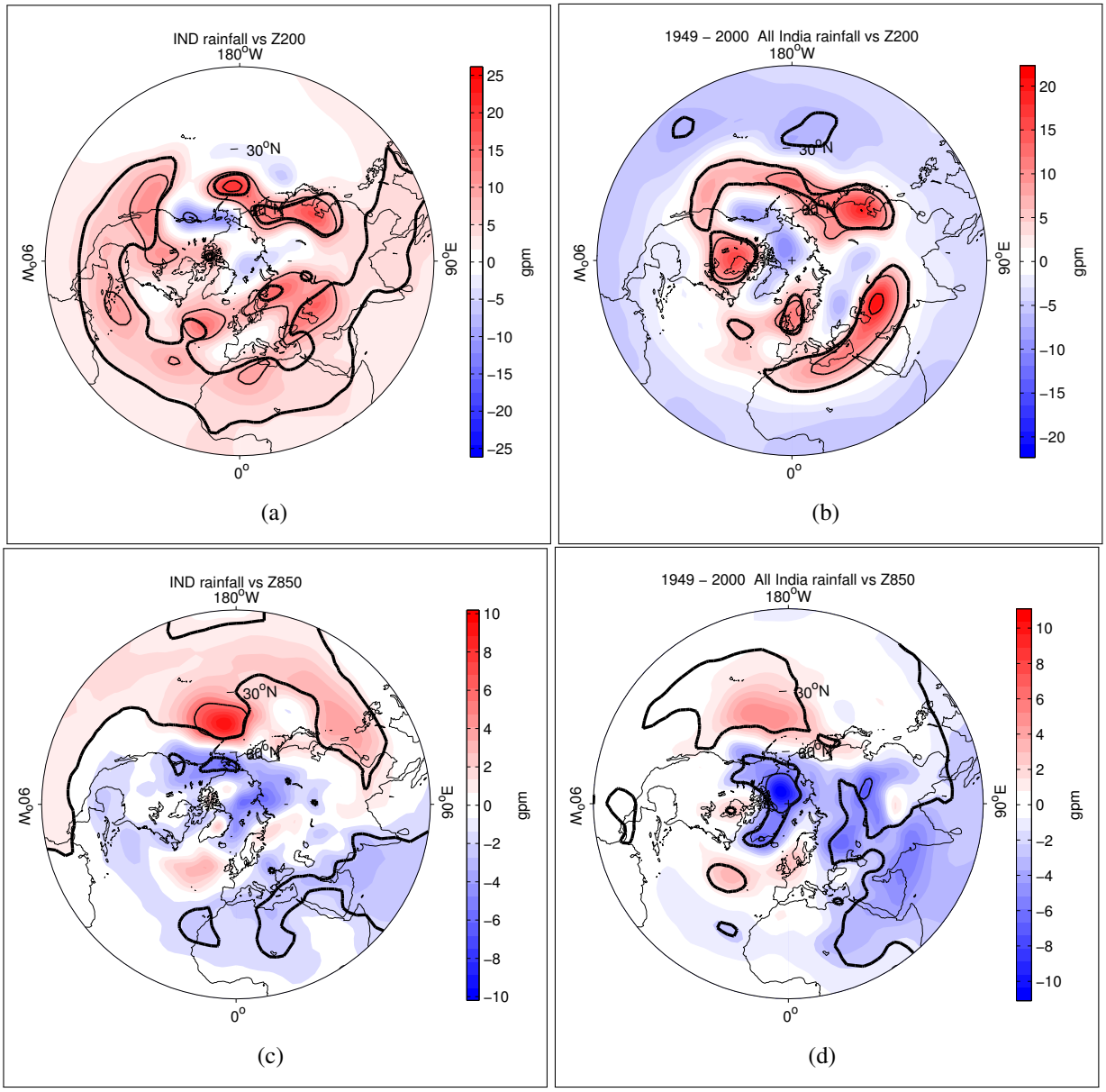

Figure 33: JJAS IND rainfall regressed on (a) Z200, (c) Z850. 1949 - 2000 All India Rainfall Index regressed on (b) Z200, (d) Z850. Contour interval is 10 gpm in (a) and (b), 6 gpm in (c) and (d). Negative (positive) values are blue (red). The bold solid line marks the 95% confidence level of the regression slope. The JJAS IND rainfall time series, as well as the All India Rainfall is shown in Figure 10.

state that the ISM teleconnections are robust even if ENSO is not removed. In the case of All India rainfall, we removed the NCEP/NCAR rainfall time series in the Nino3.4 box in the period of 1949 - 2000. We note that in the period of overlap (1980 - 2011), JJAS mean NCEP/NCAR rainfall in the Nino3.4 box is highly correlated with the satellite ensemble mean rainfall in that region (r = 0.84, see comparison in Figure 2). The regressions shown in Figure 33, as all other regressions presented here, correspond to an extra rainfall of one standard deviation of rainfall in the period of interest. The standard deviation of All India rainfall in 1949-2000 is 0.68 mm/day, which compares well with 0.65 mm/day for 1980 - 2011 in our satellite ensemble mean.

In the polar projection of anomalous Z200 (Figure 33 (a) and (b)), the circumglobal character of the teleconnection between 35°and 55°N is revealed. There are mainly four clearly separated centers of this teleconnection, one over Central West India, which extends westward, well over North Africa, one over the central Atlantic, one over Central North America, and one over Korea, which extends eastward well into the Pacific sector. This circumglobal teleconnection was described in detail in Ding and Wang (2005). One point, which is different in our analysis compared to Ding and Wang (2005) is that they find five separated centers of action, while we find four. The reason is that the Center over Korea in the study of Ding and Wang (2005) is decoupled from the part in the north-western Pacific. However, we find this pattern also when using the All India rainfall index as an estimate for India rainfall, even over the whole available period from 1949 - 2000. This underlines the robustness of the link between the ISM and the circumglobal teleconnection. One would not necessarily expect the nature of the teleconnection to be a stationary feature. For example, Greatbatch et al. (2004) found that the ENSO-related teleconnection over Eurasia is not stationary, and even changed its sign after 1979.

As pointed out by Ding and Wang (2005), the circumglobal teleconnection pattern in the upper troposphere is significantly resembling the second EOF of Northern hemisphere Z200. In Figure 34 we show the second EOF of 1980 - 2011 JJAS Z200 from our analysis. The similarity to the patterns in Figure 33 a) and b) in midlatitudes is striking, as well as the fact that these disturbances are located at the vicinity of the mid latitude jet. The PC time series shown in Figure 34 is correlated with the IND rainfall at 0.39 (significant at the 95% confidence level).

The mechanism proposed by Ding and Wang (2005) to excite this teleconnection pattern arises from the diabatic heating due to rainfall variability over India during the ISM, which induces planetary wave driving. There are several classical studies to show how ISM heating can generate a Gill- Type Rossby wave response (Gill, 1980, Rodwell and Hoskins, 1996, for example). Notable is the positive Z200 anomaly over west central Asia (see Fig. 33), that extends further east over North Africa. Ding and Wang (2005), using a linear model to investigate ISM teleconnections, claim it is probably forced directly by the ISM heating to its east. In our analysis, it is accompanied by another anticyclonic response over southern Africa (not shown), indicative of an equator-symmetric part of the response. Lin (2009) also finds the positive Z200 anomaly over west central Asia as the atmospheric response to ISM heating in a linear model (his Figure 9 a)). We thus conclude that the enhanced Western Asian high, as well as the positive anomaly over China,

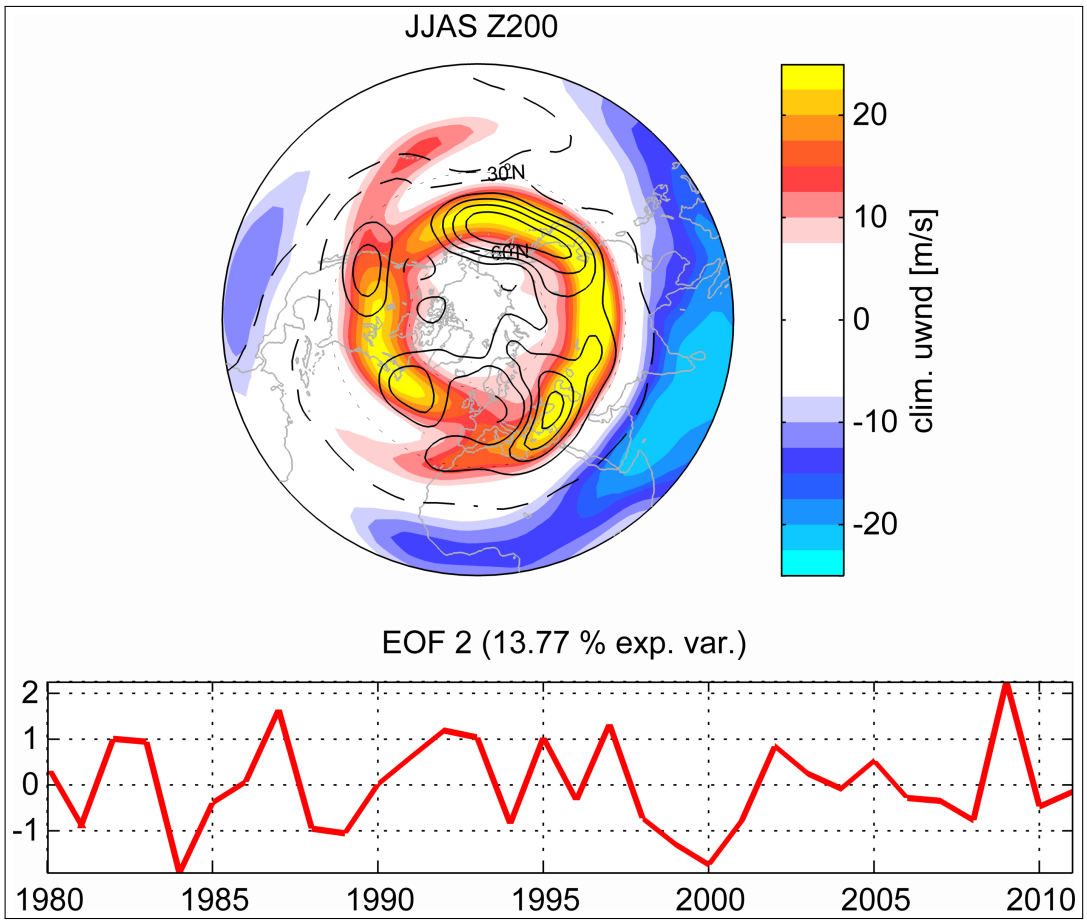

Figure 34: top panel: Contours show second EOF of northern hemisphere JJAS Z200 in the period 1980 - 2011. Contour interval is 5 gpm, zero line is left out. Negative values are dashed. Colour shading is the climatological JJAS zonal wind in 200 hPa. **bottom panel**: the corresponding PC time series and explained variance of EOF2.

are very likely direct linear responses to the diabatic heating of the ISM.

In Figure 33 (c) and (d), the Z850 teleconnections of the ISM are provided. They are substantially different from the Z200 analysis. In Z850, a significant positive anomaly is apparent over the northern Pacific, between 30°and 60°N. In Figure 33 (c), one can also identify a significant positive anomaly, that extends from southeast China to the Philippines. On the other hand side, the polar region and the whole Indian region are governed by a negative anomaly, which extends eastward over northern Africa. In particular, the eastern Mediterranean and the eastern part of the Sahara are covered by negative Z850 anomalies. All the mentioned Z850 features are consistent between the two rainfall estimates (satellite ensemble mean and All India rainfall index) and in the following, they will be used to briefly illustrate the far-reaching impacts of the ISM teleconnection on climate.

6.1. Impacts of the ISM teleconnection

Since the atmospheric circulation pattern, that is related to strong rainfall during the ISM, is of global scale, it has far reaching influence on atmospheric processes, not only at upper tropospheric levels, but also near the surface. In particular, the ISM significantly affects rainfall in widely separated points throughout the globe. In the following, the importance of the ISM - generated teleconnection pattern shall be underlined by examining the remote impact towards two separate regions.

The ISM - Sahara/Mediterranean link

In the observational and modelling climate community, two prominent features are well documented regarding the remote impact of Indian monsoon rainfall on the North African and Mediterranean sector. First, above average rainfall during the ISM goes along with enhanced rainfall in the Sahel/Sahara region (Kraus, 1977, Ward, 1998, Raicich et al., 2003, for example). This relation is of particular interest in the context of the observed downward trend in ISM rainfall (Bollasina et al., 2011) and ongoing desertification in North Africa (Nicholson et al., 1998, Haarsma et al., 2005).

On the other hand, strong ISM rainfall goes along with (and possibly might even lead to) decreased rainfall and SLP in the Mediterranean (Rodwell and Hoskins, 1996, Raicich et al., 2003). These relations shall be investigated in the following.

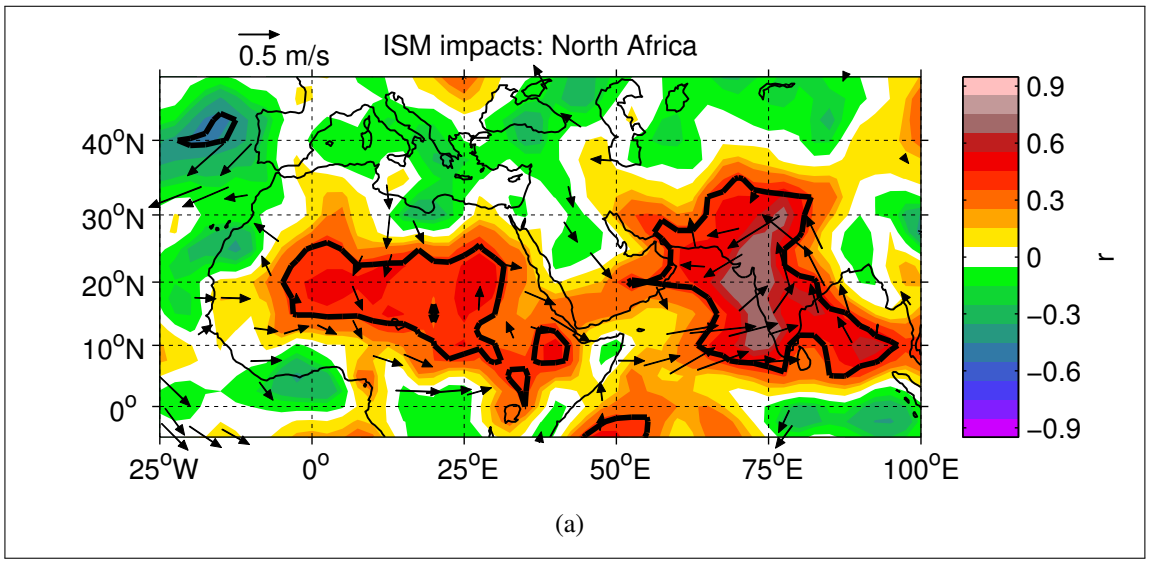

Figure 35: North Africa: correlation coefficient between JJAS IND rainfall and local rainfall (colour contours). Colour contouring in steps of 0.1. Black line indicates the 95% confidence interval of the correlation. Arrows show horizontal winds at 850 hPa height regressed on IND rainfall. Only significant (95%) wind anomalies are plotted. The anomalous winds correspond to one standard deviation of the detrended IND rainfall.

We already showed that IND rainfall is significantly correlated to Sahel rainfall in JJAS (r = 0.56, see Table 2). Figure 35 further shows the JJAS correlation coefficient between IND rainfall and local rainfall in the displayed domain. The significant positive correlation with Sahel/Sahara rainfall is clearly revealed ($r \approx 0.5$). The aforementioned negative correlation in the Mediterranean region is only very spurious and not significant in JJAS (strongest negative correlations of -0.3). However, the negative correlation coefficients over the eastern Mediterranean are more pronounced in JAS (not shown), which is consistent with Raicich et al. (2003). Figure 33 and 35 are used to explain the India-Sahel/Mediterranean link. The Z200 signals over northern Africa and the Mediterranean are very similar and consist of a tongue of positive response, reaching from India to the subtropical Atlantic. This is in good agreement with Lin (2009, his figure 7b) and Rodwell and Hoskins (1996, their figure 8). The latter authors suggest a dynamical connection between these regions and even argue that the process which connects these regions may be responsible for desertification. In their study, a Rossby wave is excited via strong diabatic heating over India, propagating westwards. They claim that interaction of this Rossby wave with the southern flank of the midlatitude westerlies leads to adiabatic descent, which occurs over the Mediterranean and the eastern Sahara. Indeed, when looking at the upper panel in Figure 33, an anticyclonic anomaly over North Africa and the Mediterranean is clearly identified. From this point of view, reduced rainfall in the region of adiabatic descent seems consistent. However, Rodwell and Hoskins (1996) state that their findings do not simply correspond to a strengthened Hadley cell, since the descending air has midlatitude origin.

The Z850 regressions in Figure 33 reveal a negative anomaly over the eastern Sahara and Mediterranean. Further, in Figure 35, anomalous 850 hPa winds are shown, that go along with above average IND rainfall. Apart from the cyclonic feature over the Indian subcontinent, which is consistent with the ISM heating, two features over northern Africa are identified. There is significant westerly flow towards northern Africa from the Atlantic between 10°and 20°N and significant southward flow towards northern Africa from the Mediterranean at about 15°E. Both of these features potentially advect more moist marine air from the subtropical Atlantic and the Mediterranean towards the Sahel/Sahara region, which leads to enhanced rainfall there. Compared with the Z850 regression maps in Figure 33 (c) and (d), these anomalous winds may be viewed as the geostrophic component of the ISM teleconnection over northern Africa. They could partially explain the positive rainfall correlations with the ISM in the Sahel/Sahara region, that were unrevealed in Figure 35.

The ISM - North China link

A prominent teleconnection emerging from strong Indian summer monsoon is an anticyclonic anomaly over north east China in upper tropospheric levels (Wang et al., 2001, Lin, 2009, Sun et al., 2010), which has also been found in this thesis (see Figure 33). Regarding lower tropospheric levels, it has been suggested that the ISM can influence the East Asian Summer Monsoon (EASM) to yield enhanced rainfall in northern China (Wang et al., 2001, Greatbatch et al., 2013). In particular, it has been shown that the second mode of variability of the EASM is significantly correlated with the All India rainfall index (Greatbatch et al., 2013). Understanding the ISM-EASM link is crucial for climate forecasting, since both the ISM and northern China rainfall show a downward trend in recent decades (Bollasina et al., 2011, Greatbatch et al., 2013, and references therein).

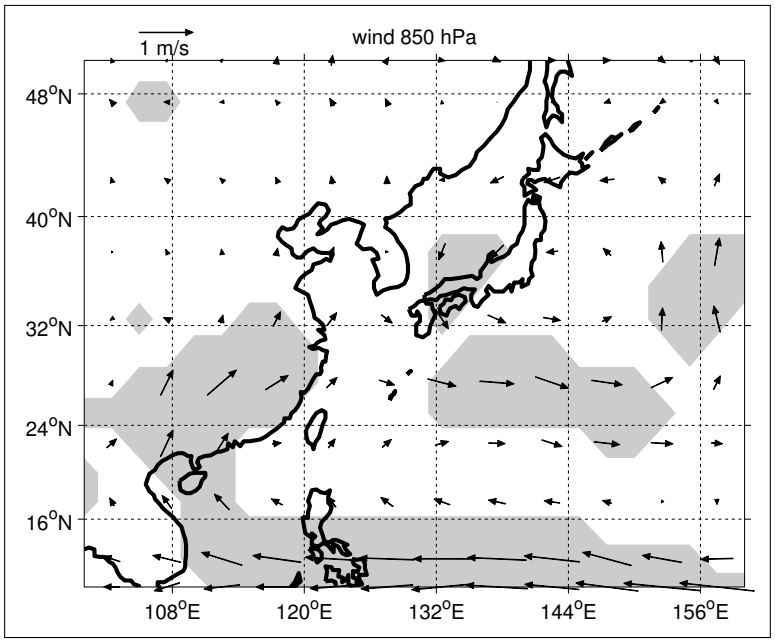

Figure 36: Northeast China: JJAS IND rainfall regressed on 850 hPa windfield. significance at the 95 % confidence level is given by the grey shading. Wind pattern corresponds to one standard deviation of the detrended IND rainfall.

Figure 36 shows anomalous 850 hPa winds that are associated with enhanced IND rainfall. One can see anomalous easterly flow over the Phillipines and northward flow over East China. This pattern is consistent with the 850 hPa wind pattern of second EOF of the EASM, as found in Sun et al. (2010). The wind pattern suggests an enhanced moisture transport from the warm waters of the western tropical Pacific towards southeast China, and a northward advection of those moist air masses over southeast China, that would perhaps lead to enhanced rainfall in north China. Although Wang et al. (2001) claim that many studies find this rainfall link, it is not apparent in this analysis in terms of JJAS mean rainfall. This was the motivation to also examine single month rainfall to find the strongest possible connection amongst these two regions. Maximum correlation coefficients are found at zero months lag in the individual months of June (r = 0.36) and July (r =

0.39), both significant at the 95% confidence level. Thus, the summer rainfall connection of the regions of India and Northern China in the satellite rainfall ensemble has been underlined on a statistical significant basis.

These examples illustrate how the ISM-related atmospheric teleconnections may affect rainfall at places very distant from India. They further show that the satellite ensemble mean rainfall, that was used in this thesis, is a good representation of the seasonal rainfall variability, and the associated diabatic heating, since the documented teleconnections from ISM heating could be reproduced.

7. Summary and Conclusions

In this thesis, seasonal mean rainfall is used as a proxy for diabatic heating in the atmosphere. Analysing their interannual variability, the connection between local rainfall events and anomalous atmospheric circulation patterns is investigated. The term teleconnection describes the tendency of atmospheric parameters to show parallel behaviour between widely separated points on the globe. While atmospheric teleconnection patterns are often associated with internal dynamics of the atmosphere, especially in the northern hemisphere winter, we address the question whether they may also be excited by local sources of diabatic heating due to strong interannual rainfall variability. As teleconnections affect the weather in many regions on the globe, results from this thesis may help to improve their predictability on interannual time scales, which is a matter of both scientific and socio-economic interest.

Regarding precipitation data, we use an ensemble mean product of three satellite-based rainfall estimates for the period of 1980 - 2011. The motivation for using satellite rainfall is straightforward, because rainfall estimates from gridded reanalysis products lack quality, especially over the oceans and apart from ENSO-related rainfall (Efthymiadis et al., 2005).

We find regions of strong interannual variability of both monthly mean and seasonal mean rainfall. We then average seasonal mean rainfall in those regions to yield a rainfall time series that is representative for the region of strong rainfall variability. In boreal winter (DJF mean), we investigate rainfall in the regions of topical South America, the eastern and central tropical Pacific, the Maritime Continent, the tropical Indian Ocean, the Congo and the Gulf Stream. For boreal summer (JJAS mean), the regions of Sahel, northeast China and the Indian Subcontinent are analysed.

It is found that ENSO significantly affects rainfall in many regions of the world in winter. Since we are also interested in rainfall variability and teleconnections apart from what is associated with ENSO, we removed the ENSO signal from all rainfall time series (except the eastern Pacific Nino3.4 rainfall box). Hence, our results are built upon seasonal mean, detrended rainfall estimates, with the linear effect of ENSO removed.

Except for South America and the Congo, anomalous DJF mean rainfall in all of our investigated boxes is associated with large-scale atmospheric teleconnections. In the tropics, the response to anomalous tropical rainfall is mainly given by the Gill type response. It consists of two equator-

symmetric cyclones at lower tropospheric levels (anticyclones aloft) northwest and southwest of the region of enhanced diabatic heating. Given the similarity between the linear model results of Gill (1980) and our results for the tropical response to tropical rainfall variability, we conclude that in the tropics, the satellite ensemble mean rainfall is a good proxy for the diabatic heating in the atmosphere. Furthermore, these findings suggest that the tropical response is governed by linear dynamics.

Regarding the extratropical teleconnections, it is shown that the satellite ensemble mean rainfall in the eastern Pacific significantly projects onto the positive phase of the Pacific North American (PNA) pattern and the Pacific South American (PSA) pattern. Moreover, enhanced rainfall in the Nino3.4 box is found to go along with anomalous upper tropospheric Rossby wave sources in the North Pacific and North Atlantic Oceans. These anomalies are located in the vicinity of the midlatitude jets, highlighting the potential of the jet streams to act as wave guides for triggering the extratropical teleconnection. The results also suggest a stratospheric pathway for the teleconnections emerging from anomalous heating over the tropical eastern Pacific, which is somewhat similar to what is discussed in Garfinkel et al. (2012) and Butler et al. (2014). However, the effect of Stratospheric Sudden Warmings (SSWs) additionally complicates the character of the teleconnection, and our results regarding the effect of SSWs bear a low degree of statistical significance. We conclude that the observational records are too short for a thorough analysis of the stratospheric teleconnections including the effect of SSWs, when using observational data alone.

Investigation of anomalous rainfall in the Central Pacific (CP) is motivated by the discovery of a new type of El Niño in recent decades (Ashok et al., 2007, Ashok and Yamagata, 2009), where anomalous convective activity shifts westward from the Nino3.4 box. Thus, CP rainfall is associated with an extratropical teleconnection that is somewhat similar to a westward shifted PNA pattern and, although not significant at the 95% confidence level, it projects onto the negative phase of the North Atlantic Oscillation (NAO). It is found that the westward shifted PNA pattern is related to anomalous positive RWSs in the upper troposphere over the western-central Pacific.

It is shown that Maritime Continent (MC) rainfall is dominated by low frequency decadal variability, when the effect of ENSO is removed. The extratropical teleconnections associated with enhanced MC rainfall consist of two wavetrains, that spread northeastward and southeastward from the MC. An impact on European climate is suggested via a weak projection onto the NAO. The generation of those teleconnections is consistent with anomalous RWSs over Thailand, China

and Mexico. Despite the high negative correlation between ENSO and MC rainfall, we emphasize that the MC rainfall teleconnection pattern is substantially different from the inverse of the pattern that we found for diabatic heating over the eastern Pacific.

Interannual winter time rainfall variability over the tropical Indian Ocean (IO) is associated with the Madden Julian Oscillation (MJO). We find a strong projection of IO rainfall on the NAO (r = 0.55), which is in concert with other studies (e.g. Hoerling et al., 2001, Copsey et al., 2006, Cassou, 2008, Lin et al., 2015). We suggest IO rainfall forces a Rossby wave train over the western-central North Pacific, which is generated by anomalous RWSs over eastern Eurasia. Anomalous positive RWSs between Greenland and Hudson Bay are responsible for the link between enhanced IO rainfall and the NAO. In contrast to the model studies of Hoerling et al. (2001) and Bader and Latif (2005), we do not find that enhanced DJF mean IO rainfall is associated with enhanced IO SSTs. This points towards the importance of the diabatic heating in the atmosphere over the IO to drive global teleconnections, rather than interannual SST variability.

Enhanced DJF mean rainfall over the Gulf Stream (GU) projects on wavenumber two activity in the polar regions of the northern hemisphere. Moreover, a negative RWS anomaly is found over Cape Hatteras in the Atlantic jet stream core, indicating divergence. This RWS anomaly is associated with a wave train spreading eastward over the Atlantic Ocean and Eurasia, bearing similarities to the circumglobal wave train at the northern edge of the midlatitude jet stream, as found in Branstator (2002).

Regarding northern hemisphere summer (JJAS), enhanced rainfall during the Indian Summer Monsoon (ISM) is shown to generate a circumglobal upper tropospheric response in the northern hemisphere. This circumglobal teleconnection significantly resembles the second mode of variability of the northern hemisphere Z200 in summer, and it consists of disturbances along the midlatitude jet stream. This result could be reproduced by using an independent ISM rainfall data set (Parthasarathy et al., 1995). We emphasize the importance of the ISM teleconnection for the global climate by investigating its dynamical connection to rainfall in northern Africa and northeast China.

Overall, the satellite ensemble mean rainfall product is shown to be a good proxy for diabatic heating in the atmosphere, since most of the prominent teleconnections associated with tropical and extratropical diabatic heating could be reproduced. We note that this was not the case when

using gridded NCEP/NCAR reanalysis rainfall data, due to their lack in quality in many regions of the world. It is noteworthy, that the above results of this thesis are valid in the absence of the ENSO signal, and in the case of IO rainfall, even in the absence of the underlying SST signal.

8. Acknowledgements

NCEP/NCAR Reanalysis Derived data, GPCP and CMAP precipitation data provided by the NOAA/OAR/ESRL PSD, Boulder, Colorado, USA, from their Web site at http://www.esrl.noaa.gov/psd/.

I wish to express gratitude to Prof. Dr. Richard Greatbatch and Prof. Dr. Katja Matthes for supervising me during this thesis.

A special thanks to Prof. Dr. Richard Greatbatch and Gereon Gollan, who offered me this interesting topic in the first place and who constantly helped to improve the final stage of this thesis by the numerous discussions that we had.

Thanks also to Ralf. His impeccable profound pieces of advice valorized intricate data.

The final form of this thesis also benefited from the helpful suggestions of Svenja, Sebastian, Till and Felicitas.

Finally, I am grateful to my parents, who supported me during the entire time of my studies.

References

Adler, R., Huffman, G., Chang, A., Ferraro, R., Xie, P., Janowiak, J., Rudolf, B., Schneider, U., Curtis, S., Bolvin, D., Gruber, A., Susskind, J., , and Arkin, P. (2003). The Version 2 Global Precipitation Climatology Project (GPCP) Monthly Precipitation Analysis (1979-Present). *J. Hydrometeor.*, 4:1147–1167.

Arkin, P. A. and Meisner, B. N. (1987). The relationship between large-scale convective rainfall and cold cloud over the western hemisphere during 1982-84. *Mon. Wea. Rev.*, 115:51–74.

Ashok, K., Behera, S. K., Rao, S. A., Weng, H., and Yamagata, T. (2007). El Niño Modoki and its possible teleconnection. *Geophys. Res.*, 112(C11007).

Ashok, K. and Yamagata, T. (2009). The El Niño with a difference. *Nature*, 461:481–484.

Bader, J. and Latif, M. (2005). North Atlantic Oscillation Response to Anomalous Indian Ocean SST in a Coupled GCM. *J. Climate*, 18:5382–5389.

Barnston, A. G. and Livezey, R. E. (1987). Classification, Seasonality and Persistence of Low-Frequency Atmospheric Circulation Patterns. *Mon. Wea. Rev.*, 115:1083–1126.

Blackmon, M. (1976). A climatological spectral study of 500 mb geopotential height of the northern hemisphere. *Journal of the Atmospheric Sciences*, 33:1607–1623.

Bollasina, M. A., Ming, Y., and Ramaswamy, V. (2011). Anthropogenic aerosols and the weakening of the South Asian summer monsoon. *Science*, 334:502–505.

Branstator, G. (2002). Circumglobal Teleconnections, the Jet Stream Waveguide, and the North Atlantic Oscillation. *J. Climate*, 15:1893–1910.

Butler, A. H., Polvani, L., and Deser, C. (2014). Separating the stratospheric and tropospheric pathways of El Niño–Southern Oscillation teleconnections. *Environ. Res. Lett.*, 9.

Cassou, C. (2008). Intraseasonal interaction between the Madden-Julian Oscillation and the North Atlantic Oscillation. *Nature*, 455:523–527.

Copsey, D., Sutton, R., and Knight, J. R. (2006). Recent trends in sea level pressure in the Indian Ocean region. *Geophys. Res. Lett.*, 33(L19712).

Ding, H., Greatbatch, R. J., and Gollan, G. (2015). Tropical impact on the interannual variability and long-term trend of the Southern Annular Mode during austral summer from 1960/1961 to 2001/2002. *Climate Dynamics*, 44(7-8):2215–2228.

Ding, Q. and Wang, B. (2005). Circumglobal teleconnection in the northern hemisphere summer. *J. Climate*, 18:3483–3505.

Efthymiadis, D., New, M., and Washington, R. (2005). On the reconstruction of seasonal oceanic precipitation in the presatellite era. *J. Geophys. Res.*, 110(D06103).

Garfinkel, C. I., Feldstein, S. B., Waugh, D. W., Yoo, C., and Lee, S. (2012). Observed teleconnection between stratospheric sudden warmings and the Madden-Julian Oscillation. *Geophys. Res. Lett.*, 39.

Gill, A. E. (1980). Some simple solutions for heat-induced tropical circulation. *Q.J.R. Meteorol. Soc.*, 106:447–462.

Gong, D.-Y., Gao, Y., Guo, D., Mao, R., Yang, J., Hu, M., and Gao, M. (2014). Interannual linkage between Arctic/North Atlantic Oscillation and tropical Indian Ocean precipitation during boreal winter. *Climate Dynamics*, 42:1007–1027.

Greatbatch, R. J. (2000). The North Atlantic Oscillation. *Stochastic Environmental Research and Risk Assessment*, 14(4+5):213–242.

Greatbatch, R. J., Lu, J., and Peterson, K. A. (2004). Nonstationary impact of ENSO on Euro-Atlantic winter climate. *Geophys. Res. Lett.*, 31(L02208).

Greatbatch, R. J., Sun, X., and Yang, X.-Q. (2013). Impact of variability in the Indian summer monsoon on the East Asian summer monsoon. *Atmosph. Sci. Lett.*, 14:14–19.

Haarsma, R. J., Selten, F. M., Weber, S. L., and Kliphuis, M. (2005). Sahel rainfall variability and response to greenhouse warming. *Geophys. Res. Lett.*, 32(L17702).

Held, I. M., Ting, M., and Wang, H. (2002). Northern Winter Stationary Waves: Theory and Modeling. *J. Climate*, 15:2125–2144.

Hoerling, M., Hurrell, J., Xu, T., Bates, G., and Phillips, A. (2004). Twentieth century North Atlantic climate change. Part II: Understanding the effect of Indian Ocean warming. *Climate Dynamics*, 23:391–405.

Hoerling, M. P., Hurrell, J. W., and Xu, T. (2001). Tropical Origins for Recent North Atlantic Climate Change. *Science*, 292(5514):90–92.

Hoskins, B. J. and Ambrizzi, T. (1993). Rossby Wave Propagation on a Realistic Longitudinally Varying Flow. *J. Atmos. Sci.*, 50:1661–1671.

Hoskins, B. J. and Karoly, D. J. (1981). The steady linear response of a spherical atmosphere to thermal and orographic forcing. *J. Atmos. Sci.*, 38:1179–1196.

Hurrell, J., Kushnir, Y., Ottersen, G., and Visbeck, M. (2003). An Overview of the North Atlantic Oscillation. *The North Atlantic Oscillation: Climatic Significance and Environmental Impact. Geophysical Monograph*, 134.

Hurrell, J. W. (1995). Decadal Trends in the North Atlantic Oscillation: Regional Temperatures and Precipitation . *Science*, 269(5224):213–242.

Ineson, S. and Scaife, A. A. (2009). The role of the stratosphere in the European climate response to El Niño. *Nature Geoscience*, 2:32–36.

Janowiak, J. E. and Xie, P. (1999). CAMS/OPI: a global satellite-raingauge merged product for real-time precipitation monitoring applications. *J. Climate*, 12:3335–3342.

Jung, T., Hilmer, M., Ruprecht, E., Kleppek, S., Gulev, S. K., and Zolina, O. (2003). Characteristics of the Recent Eastward Shift of Interannual NAO Variability. *J. Climate*, 13:3371–3382.

Kalnay, E., Kanamitsu, M., Kistler, R., Collins, W., Deaven, D., Gandin, L., Iredell, M., Saha, S., White, G., Woollen, J., Zhu, Y., Leetmaa, A., Reynolds, R., Chelliah, M., Ebisuzaki, W., Higgins, W., Janowiak, J., Mo, K. C., Ropelewski, C., Wang, J., Jenne, R., and Joseph, D. (1996). The NCEP/NCAR 40-Year Reanalysis Project. *Bull. Amer. Meteor. Soc.*, 77:437–471.

Kraus, E. B. (1977). Subtropical Droughts and Cross-Equatorial Energy Transports. *Mon. Wea. Rev.*, 105:1009–1018.

L'Heureux, M. L. and Higgins, R. W. (2008). Boreal Winter Links between the Madden–Julian Oscillation and the Arctic Oscillation. *J. Climate*, 21:3040–3050.

Lin, H. (2009). Global extratropical response to diabatic heating variability of the asian summer monsoon. *J. Atmos. Sci.*, 66:2697–2713.

Lin, H., Brunet, G., and Derome, J. (2009). An observed connection between the North Atlantic Oscillation and the Madden-Julian Oscillation. *J. Climate*, 22:364–380.

Lin, H., Brunet, G., and Yu, B. (2015). Interannual variability of the Madden-Julian Oscillation and its impact on the North Atlantic Oscillation in the boreal winter. *Geophys. Res. Lett.*, 42.

Lu, J. and Greatbatch, R. J. (2002). The changing relationship between the NAO and northern hemisphere climate variability. *Geophys. res. Lett.*, 27(7).

Madden, R. A. and Julian, P. R. (1972). Description of global-scale circulation cells in the tropics with a 40–50 day period. *J. Atmos. Sci.*, 29:1109–1123.

Matsuno, T. (1970). Vertical propagation of stationary planetary waves in the winter northern hemisphere. *J. Atmos. Sci.*, 27:871–883.

Minobe, S., Kuwano-Yoshida, A., Komori, N., Xie, S.-P., and Small, R. J. (2008). Influence of the Gulf Stream on the troposphere. *Nature*, 452:206–209.

Mitovski, T. and Folkins, I. (2014). Anomaly patterns about strong convective events in the tropics and midlatitudes: Observations from radiosondes and surface weather stations. *J. Geophys. Res. Atmos.*, 119:385–406.

Mo, K. C. and Peagle, J. N. (2001). The Pacific-South American Modes and their downstream effect. *International Journal of Climatology*, 21:1211–1229.

Nicholson, S. E., Tucker, C. J., and Ba, M. B. (1998). Desertification, Drought, and Surface Vegetation: An Example from the West African Sahel. *Bull. Amer. Meteor. Soc.*, 79(5):815–829.

Parthasarathy, B., Munot, A., and Kothawale, D. (1995). Monthly and seasonal rainfall series for All-India homogeneous regions and meteorological subdivisions: 1871-1994. *Contributions from Indian Institute of Tropical Meteorolgy, Research Report RR-065*.

Poccard, I., Janicot, S., and Camberlin, P. (2000). Comparison of rainfall structures between NCEP/NCAR reanalyses and observed data over tropical Africa. *Climate Dynamics*, 16(12):897–915.

Raicich, F., Pinardi, N., and Navarra, A. (2003). Teleconnections between Indian monsoon and Sahel rainfall and the Mediterranean. *Int. J. Climatol.*, 23:173–186.

Ratcliffe, R. A. S. and Murray, R. (1970). New lag association between North Atlantic sea surface temperature and European pressure applied to long range weather forecasting. *Quartly. J. Roy. Met. Soc.*, 96:226–246.

Rodwell, M. J. and Folland, C. K. (2002). Atlantic air–sea interaction and seasonal predictability. *Quartly. J. Roy. Met. Soc.*, 128:1413–1443.

Rodwell, M. J. and Hoskins, B. J. (1996). Monsoons and the dynamics of deserts. *Q.J.R. Meteorol. Soc*, 122:1385–1404.

Ropelewski, C. F. and Halpert, M. S. (1987). Global and Regional Scale Precipitation Patterns Associated with the El Niño/Southern Oscillation. *Mon. Wea. Rev.*, 115:1606–1626.

Sardeshmukh, P. D. and Hoskins, B. J. (1988). The generation of global rotational flow by steady idealized tropical divergence. *J. Atmos. Sci.*, 45:1228–1251.

Sun, X., Greatbatch, R. J., Park, W., and Latif, M. (2010). Two major modes of varibility of the East Asian summer monsoon. *Q.J.R. Meteorol.Soc.*, 136:829–841.

Todd, M. and Washington, R. (1999). A simple method to retrieve 3-hourly estimates of global tropical and subtropical precipitation from international satellite cloud climatology program (ISCCP) D1 data. *J. Atmos. Oceanic Technol.*, 16:146–155.

Trenberth, K. E., Branstator, G. W., Karoly, D., Kumar, A., Lau, N.-C., and Ropelewski, C. (1998). Progress during TOGA in understanding and modeling global teleconnections associated with tropical sea surface temperatures. *J. Geophys. Res.*, 103:14291–14324.

von Storch, H. and Zwiers, F. W. (1999). Statistical Analysis in Climate Research. *Cambridge University Press, Cambridge*, (ISBN: 9780521012300):x+484pp.

Walker, G. T. and Bliss, E. W. (1932). World Weather V. *Mem. Roy. Meror. Soc.*, 4:53–84.

Wallace, J. M. and Gutzler, D. S. (1981). Teleconnections in the geopotential height field during the northern hemisphere winter. *Mon. Wea. Rev.*, 109:784–812.

Wang, B., Wu, R., and Lau, K.-M. (2001). Interannual Variability of the Asian Summer Monsoon: Contrasts between the Indian and the Western North Pacific–East Asian Monsoons. *J. Climate*, 14:4073–4090.

Ward, M. N. (1998). Diagnosis and Short-Lead Time Prediction of Summer Rainfall in Tropical North Africa at Interannual and Multidecadal Timescales. *J. Climate*, 11:3167–3191.

Webster, P. J. and Holton, J. R. (1982). Wave Propagation Through a Zonally Varying Basic Flow: The Influences of Mid-Latitude Forcing in the Equatorial Regions. *J. Atmos. Sci.*, 39:722–733.

Weng, H., Behera, S. K., and Yamagata, T. (2009). Anomalous winter climate conditions in the Pacific rim during recent El Niño Modoki and El Niño events. *Clim. Dyn.*, 32:663–674.

Wheeler, M. C. and Hendon, H. H. (2004). An All-Season Real-Time Multivariate MJO Index: Development of an Index for Monitoring and Prediction. *Mon. Wea. Rev.*, 132:1917–1932.

Xie, P. and Arkin, P. (1997). Global precipitation: A 17-year monthly analysis based on gauge observations, satellite estimates, and numerical model outputs. *Bull. Amer. Meteor. Soc.*, 78:2539 – 2558.

Zhang, C. (2005). Madden-Julian Oscillation. *Rev. Geophys.*, 43(RG2003):1109–1123.

Zhang, R. and Delworth, T. L. (2006). Impact of Atlantic multidecadal oscillations on India/Sahel rainfall and Atlantic hurricanes. *Geophys. Res. Lett.*, 33.

Zhou, S. and Miller, A. J. (2005). The Interaction of the Madden–Julian Oscillation and the Arctic Oscillation. *J. Climate*, 18:143–159.

ERKLÄRUNG

Hiermit erkläre ich, dass ich die vorliegende Arbeit selbständig und ohne fremde Hilfe angefertigt und keine anderen als die angegebenen Quellen und Hilfsmittel verwendet habe. Die eingereichte schriftliche Fassung der Arbeit entspricht der auf dem elektronischen Speichermedium.

(Name der Datei: Dahlke_954253.pdf)

Weiterhin versichere ich, dass diese Arbeit noch nicht als Abschlussarbeit an anderer Stelle vorgelegen hat.

_____

Datum, Unterschrift